The transcriptional regulator of the chaperone response HSF1 controls hepatic bioenergetics and protein homeostasis

Aijun Qiao,[1,2]* Xiongjie Jin,[1,2]* Junfeng Pang,[1,2] Demetrius Moskophidis,[1,2,3] and Nahid F. Mivechi[1,2,4]

[1]Molecular Chaperone Biology, Medical College of Georgia, [2]Georgia Cancer Center, [3]Department of Medicine, and [4]Department of Radiology, Augusta University, Augusta, GA 30912

Metabolic energy reprogramming facilitates adaptations to a variety of stress conditions and cellular dysfunction, but how the energetic demands are monitored and met in response to physiological stimuli remains elusive. Our data support a model demonstrating that heat shock factor 1 (HSF1), a master transcriptional regulator of the chaperone response, has been coopted from its role as a critical protein quality-control regulator to having a central role in systemic energy sensing and for metabolic adaptation to nutrient availability. We found that in the absence of HSF1, levels of NAD^+ and ATP are not efficiently sustained in hepatic cells, largely because of transcriptional repression of nicotinamide phosphoribosyltransferase in the NAD^+ salvage pathway. Mechanistically, the defect in NAD^+ and ATP synthesis linked to a loss of NAD^+-dependent deacetylase activity, increased protein acetylation, and impaired mitochondrial integrity. Remarkably, the drop in ATP level caused by HSF1 loss invoked an adaptive response featuring the inhibition of energetically demanding processes, including gluconeogenesis, translation, and lipid synthesis. Our work identifies HSF1 as a central regulator of cellular bioenergetics and protein homeostasis that benefits malignant cell progression and exacerbates development of metabolic diseases.

Introduction

Changes in global bioenergetics and metabolic state, particularly starvation or nutrient overload, place a high demand on energy sources and protein quality-control mechanisms of the cell and have profound effects on organismal health. Mitochondria are essential organelles for the preservation of cellular bioenergetics given their established role in energy generation via respiration, a process that requires coordinated interaction of protein subunits encoded by mitochondrial and nuclear DNA (Wallace, 2005; Liesa and Shirihai, 2013), synthesis of metabolites, and regulation of signaling pathways. Indeed, compromised mitochondrial function caused by disruption of energy production and metabolic signal integration as well as increased oxidative stress is one of the hallmarks of numerous age-related neurologic and metabolic disorders (Wallace, 2005; Koopman et al., 2012).

Protein quality-control mechanisms, including translation and protein folding, and metabolic pathways such as gluconeogenesis and lipid synthesis are the most energy-demanding processes in most organisms and present a large burden to ATP and NAD^+ supplies. For example, in differentiating mammalian cells, translation and gluconeogenesis are estimated to account for 25–30% and 7–10% of total ATP consumption, respectively (Buttgereit and Brand, 1995; Rolfe and Brown, 1997). In general, the architectures of several signaling and metabolic pathways have been considered to be robust against variations in energy supply and protein levels, and the cell has fail-safe mechanisms to adjust its catalytic capacity to cope with this challenge. Under pathological increase of metabolic and protein synthesis demands, however, this tremendous energy cost, in turn, can compromise the mitochondrial integrity and functional capacity to maintain energy homeostasis and fulfill the biosynthetic and metabolic bioenergetic needs of the cell. The fundamental question is how cells sense energetic demands and regulate the bioenergetic networks to balance the contrasting anabolic and catabolic needs under physiological and stress/disease conditions. Although tissue-specific differences in bioenergetic efficiency (e.g., brown adipose tissues, muscle or

*A. Qiao and X. Jin contributed equally to this paper.

Correspondence to Nahid F. Mivechi: nmivechi@augusta.edu; or Demetrius Moskophidis: dmoskofidis@augusta.edu

Abbreviations used: AMPK, AMP-activated protein kinase; AR, aspect ratio; BN, blue native; ChIP, chromatin immunoprecipitation; ECAR, extracellular acidification rate; ETC, electron transport chain; FAO, fatty acid oxidation; FCCP, fluoro-carbonyl-cyanide phenylhydrazone; FSK, forskolin; HSF, heat shock factor; MC, mitochondrial complex; mtDNA, mitochondrial DNA; NA, nicotinic acid; NAM, nicotinamide; NAMPT, nicotinamide phosphoribosyltransferase; NMN, nicotinamide mononucleotide; NR, nicotinamide riboside; OCR, oxygen consumption rate; OXPHOS, oxidative phosphorylation; PARP, poly(ADP-ribose) polymerase; PKA, protein kinase A; PTT, pyruvate tolerance test; TRP, tryptophan; WT, wild type.

The Rockefeller University Press $30.00
J. Cell Biol. Vol. 216 No. 3 723–741
https://doi.org/10.1083/jcb.201607091

β cells; Liesa and Shirihai, 2013) are reasonably understood, the means of complex regulatory networks by which tissue and nutrient-dependent intracellular NAD^+ and ATP pools are monitored and their integration within the larger set of protein quality-control and metabolic reprogramming mechanisms remains poorly defined.

Here, we investigated hepatic homeostatic energy-sensing mechanisms adjusting the rate of anabolic metabolic pathways to intracellular energy state, thereby allowing the metabolic capacity to readily adapt to challenging nutritional conditions. We show that heat shock factor 1 (HSF1), a key regulator of the classical chaperone response to cope with the increased protein load and protein folding defects caused by genetic abnormalities especially in malignant cells (Dai et al., 2007; Akerfelt et al., 2010; Anckar and Sistonen, 2011; Jin et al., 2011), also has critical function as an information hub for anabolic metabolic and bioenergetics and protein synthesis pathways in the cell.

Results

HSF1 is essential for maintenance of optimal NAD^+ and ATP pools in hepatic cells

A causal link between metabolism and protein homeostasis driven by HSF1 with respect to adaptive responses of the cell to energy stress has been proposed (Hahn et al., 2004; Jin et al., 2011; Santagata et al., 2013; Su et al., 2016), but knowledge of the underlying mechanisms that integrate them is lacking. We have reported that global *hsf1* deletion induces a cellular energy deficit associated with increased basal and insulin-induced AMP-activated protein kinase (AMPK) activation (Jin et al., 2011). This observation prompted us to investigate further the metabolic consequences on ATP and NAD^+ systems, focusing on liver cell bioenergetics. In this study, we used mice with whole-body gene deletion (*hsf1*$^{-/-}$; Zhang et al., 2002). To investigate the function of HSF1 in liver metabolism, we also generated a hepatocyte-specific *hsf1* knockout model (L-*hsf1*$^{-/-}$ hereafter) by crossing albumin-Cre mice (Postic et al., 1999) with *hsf1*$^{f/f}$ mice, which were functionally wild type (WT; Fig. S1). Surprisingly, we found that levels of ATP were not sustained in the livers of *hsf1*$^{-/-}$ mice (Fig. 1 A). This ATP decline significantly increased the AMP level and [AMP/ATP] ratio, reflecting an increase in AMPK activity (Fig. 1 B). Because ATP production is coupled with NAD^+ availability, we also examined whether *hsf1* deletion affects the intracellular [NAD^+/NADH] ratio. Indeed, HSF1 loss in mice and hepatic cells decreased the cellular NAD^+ bioavailability with maximal effects on mitochondrial NAD^+ levels, but it did not significantly affect NADH levels (Fig. 1, C and D). The change in NAD^+ level translated to a decreased mitochondrial [NAD^+/NADH] ratio, suggesting an organelle-specific HSF1-dependent effect on NAD^+ biosynthesis and/or consumption. Notably, the effects on cellular energy charge ([ATP], [AMP/ATP], [NAD^+], and [NAD^+/NADH]) were particularly evident in fasted livers but also detected in primary hepatocytes.

HSF1 controls cellular NAD^+ levels by regulating the NAD^+ salvage biosynthetic pathway

NAD^+ decline could be caused by an increase in NAD-consuming enzymes, such as poly(ADP-ribose) polymerases (PARPs), CD38, sirtuins, and/or a decrease in NAD-synthesizing enzymes (Dölle et al., 2013; Cantó et al., 2015). In the absence of HSF1, global PARP activity (Adamietz, 1987), and PARP-1 or CD38 contents were not significantly affected (Fig. S2, A and B), and the activities of sirtuins were decreased (see Fig. 5). These data do not support a causal role for enhanced PARP-, CD38-, or sirtuin-mediated NAD^+ breakdown in NAD^+ decline but rather suggest that this could be mediated by alterations in NAD^+ biosynthesis.

In mammalian cells, NAD^+ synthesis occurs from diverse dietary sources, including tryptophan (TRP), nicotinic acid (NA), and nicotinamide riboside (NR; Cantó et al., 2015; Fig. 2 A). In addition, NAD^+ can be resynthesized through the NAD^+-salvage pathway that involves the conversion of nicotinamide (NAM) to nicotinamide mononucleotide (NMN) by the rate-limiting enzyme nicotinamide phosphoribosyltransferase (NAMPT) and then into NAD^+ by NMNAT1 or NMNAT3. Interestingly, the basal and nutrient-induced mRNA and the protein level of NAMPT were significantly decreased in livers of *hsf1*$^{-/-}$ mice (Fig. 2 B). The subcellular levels of NAMPT were also markedly reduced (∼40%) in fed *hsf1*$^{-/-}$ mice compared with control mice, although the mitochondria-associated NAMPT level appeared to be very low (Fig. 2 C). We validated NAMPT suppression by comparing mRNA and protein levels after treatment of hepatocytes with stress agents, including heat shock or decreasing concentration of glucose (Fig. 2, D–E), which are known to induce NAMPT expression in yeast and mammalian cells (Anderson et al., 2003; Yang et al., 2007). In addition, we tested whether HSF1 directly controls *Nampt* promoter activity and expression. Promoter analysis of mouse *Nampt* identified multiple repeats exhibiting the characteristic core motif 5′-nTTCn-3′ described as noncanonical TTC-rich binding sites for HSF1 (Guertin and Lis, 2010). Chromatin immunoprecipitation (ChIP) quantitative PCR assays confirmed specific increased HSF1 occupancy at a potential binding site at nucleotide −1,209 to −965 bp of the *Nampt* promoter in primary hepatocytes exposed to decreasing glucose concentrations (Fig. 2 F). Because nutrient levels influence transcriptional programs driven by HSF1, we also investigated HSF1 occupancy on the *Nampt* and *Hsp70* promoters in livers during fed, fasting, or refeeding conditions (Fig. 2 G). Interestingly, HSF1 binding to the *Nampt* promoter was uniform at the fed or fasted state but significantly declined with refeeding; in contrast HSF1 binding to the *Hsp70* promoter was strongly increased under the refeeding condition. In keeping with previous studies, the nuclear accumulation of the hyperphosphorylated (active) form of HSF1 fluctuated in a nutrient-dependent manner (Fig. 2 H). Consistent with a direct role of HSF1 in NAD^+ salvage, we also determined that NAM treatment in vitro and in vivo could not reverse the NAD^+ and ATP-decline or restore the diminished glucose production capacity of hepatocytes caused by HSF1 loss (Fig. 2, I and J). However overexpression of HSF1 in primary *hsf1*$^{-/-}$ hepatocytes completely restored the nutrient-induced mRNA expression of *Nampt* gene (Fig. 2 K), demonstrating an HSF1-dependent cell-intrinsic effect. Furthermore, the levels of fed or fasting-induced mRNAs encoding *Nrk1* and *Nrk2*, *Nmnat1*, *Nmnat3*, and *Nadsyn1* did not significantly differ between genotypes (Fig. S2 D). Finally, to assess whether HSF1 loss may affect redox pathways regulating the cellular NAD^+ pool, we profiled transcriptional levels of selected NAD^+-dependent enzymes. The mRNA levels of several dehydrogenases that regulate the NAD^+/NADH or $NADP^+$/NADPH redox balance, however, were either not significantly

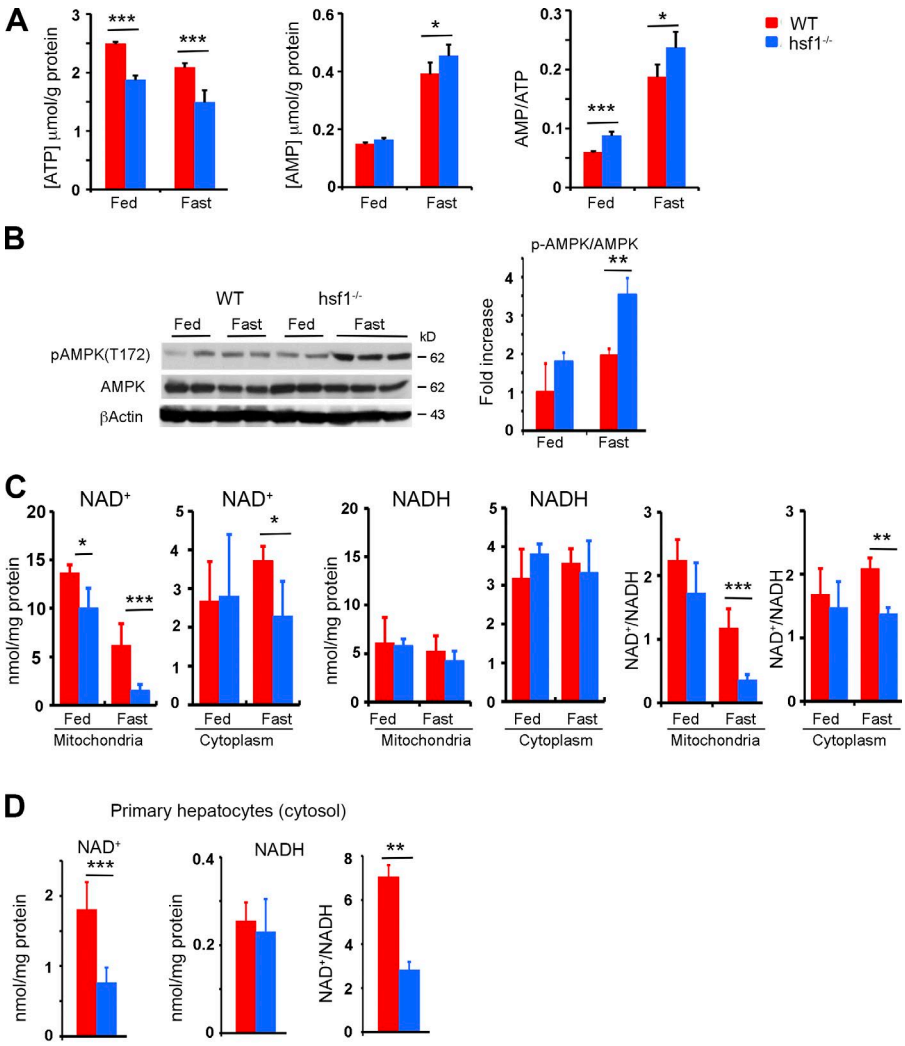

Figure 1. ***Hsf1*deletion inhibits hepatic NAD⁺ and ATP regeneration.** (A) Levels of ATP, AMP, and [AMP/ATP] ratios in livers of *hsf1*$^{-/-}$ and WT mice in a fed or 16-h fasted (fast) state. (B) Western blotting analysis of phospho-AMPK and AMPK levels in livers of *hsf1*$^{-/-}$ and WT mice in a fed or 16-h fasted state. Quantification of phospho-AMPK normalized to the total AMPK level is shown as relative to WT (fed, right). (C) Levels of NAD⁺, NADH, and [NAD⁺/NADH] ratios in livers of fed or 16-h fasted WT and *hsf1*$^{-/-}$ mice. (D) Levels of NAD⁺, NADH, and NAD⁺/NADH ratio in *hsf1*$^{-/-}$ and WT primary hepatocytes. For all panels, error bars show mean ± SD (n = 5 mice per group). *, P < 0.05; **, P < 0.01; ***, P < 0.001.

affected or decreased (Fig. S2 C). Thus, these data suggest that HSF1-mediated transcriptional regulation of *Nampt* critically impacts the intracellular NAD⁺ and ATP pools.

Effects of HSF1 on mitochondrial biogenesis and oxidative phosphorylation (OXPHOS)

Because mitochondrial biogenesis and/or electron transport chain (ETC) function have significant impact on cellular ATP production and energy status, the overall effects of HSF1 depletion on ATP and NAD⁺ contents raised two nonexclusive possibilities: first, the mitochondrial dynamics and biogenesis may be affected; and second, the reduced ATP production may be caused through a defect in mitochondrial ETC function.

We first investigated the potential effects on mitochondrial morphology and biogenesis in primary hepatocytes and livers. In addition to ATP decline, lack of HSF1 in mouse hepatocytes or HepG2 cells with *hsf1* silencing by shRNA significantly reduced the amount of mitochondrial proteins (normalized to total protein level), mass, and DNA content, indicating a general reduction in mitochondria biogenesis (Fig. 3, A–F). The mRNAs of both mitochondrial- and nuclear-encoded genes that are functionally involved in mitochondrial biogenesis (*Pgc1α*, *Pgc1β*, *Nrf1*, *Nrf2*, *Pparα*, and *ERRα*) and OXPHOS (*Nd1*, *Cox2*, *Co5b*, *Atp5j*, and *Atp6*) were present at lower levels (Fig. 3 G). Interestingly, however, changes in mRNA transcripts were seen only under fasting, which highlights a stronger contribution of HSF1 activity to cellular energy status maintenance under nutrient-limiting conditions. EM of liver tissues revealed that mitochondrial density and coverage were lower in *hsf1*$^{-/-}$ mice than WT mice in both the fed and fasted states (Fig. 3, H and I). In the fed state, these morphological changes in *hsf1*$^{-/-}$ mice were accompanied with a significant increase in the mean mitochondrial size (Fig. 3 J) but a decrease in aspect ratio (AR), indicating a more rounded shape of mitochondria (Fig. 3 K). In the fasted state, liver cells from *hsf1*$^{-/-}$ mice did not present additional significant changes in relative mitochondrial parameters other than a further increase in mitochondrial size compared with the fed condition without AR changes (Fig. 3, J and K). The morphological appearance of the enlarged mitochondria in livers of *hsf1*$^{-/-}$ mice (Fig. 3 L) is thus indicative of changes in mitochondrial fusion–fission dynamics with a trend for enhanced fusion. Because the mRNA level of genes regulating mitochondrial morphology (*Drp1*, *Mfn1*, *Mfn2*, and *Fis1*) and mitophagy (*Pink1* and *Bnip3*) did not significantly differ between genotypes (Fig. S3 A), it is unlikely that HSF1 is solely a direct and potent mRNA transcript regulator of key mitochondrial morphogenesis genes. Validation studies confirmed that levels of proteins implicated in macroautophagy (LC3-II, BEC LIN 1, p62, and BAX) and mitochondrial fusion (OPA1 and

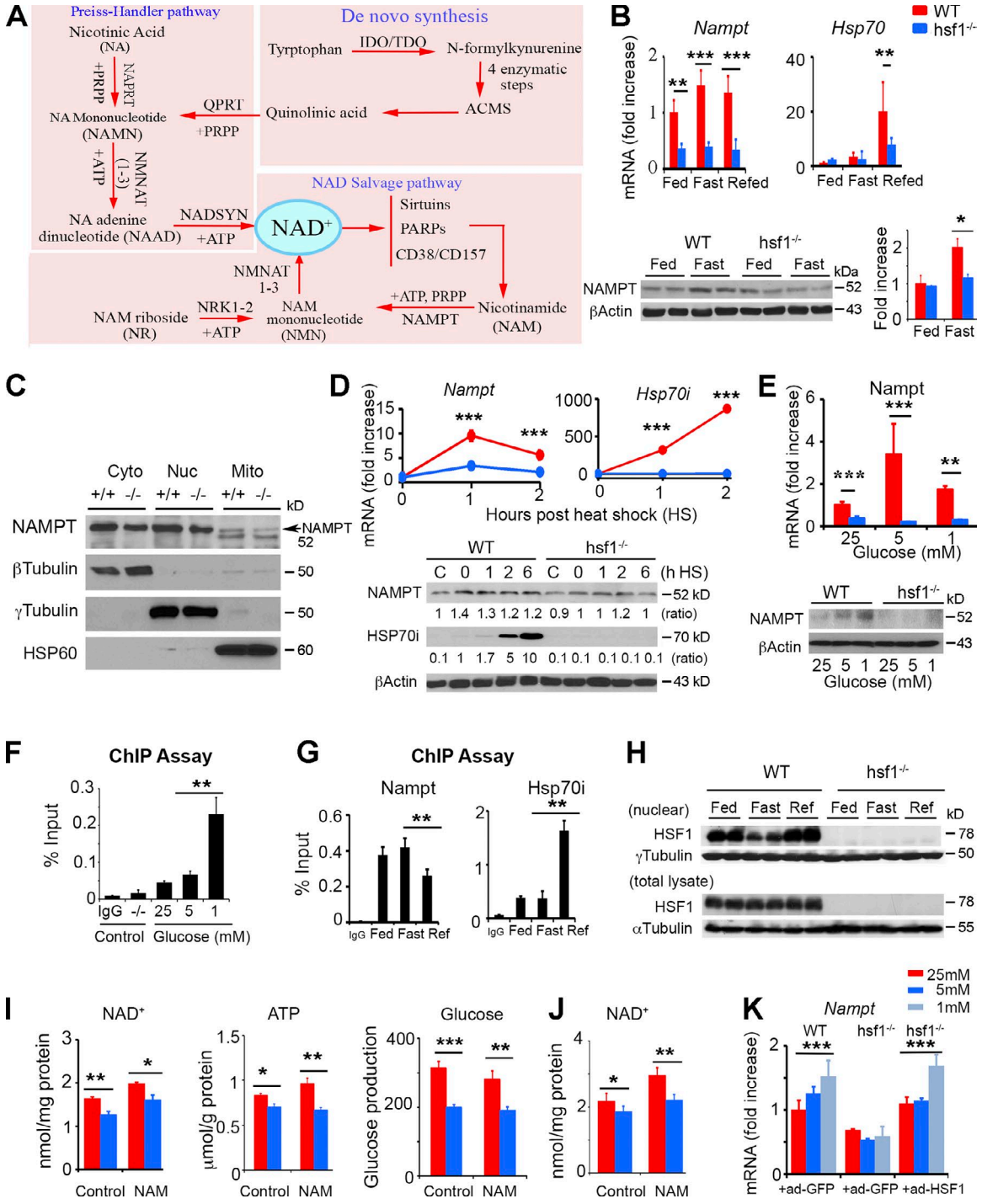

Figure 2. **HSF1-mediated regulation of NAMPT and the NAD⁺ salvage biosynthetic pathway.** (A) Diagram of NAD⁺ precursor metabolism. ACMS, α-amino-β-carboxymuconate-ε-semialdehyde; IDO, indoleamine 2,3-dioxygenase; PRPP, 5-phosphoribosyl 1-pyrophosphate; QPRT, quinolinate phosphoribosyltransferase; TDO, tryptophan 2,3-dioxygenase. (B) mRNA of *Nampt* and *Hsp70* (top) and NAMPT protein levels (bottom) in livers of fed, 24-h fasted (fast), or fasted and refed for 3 h (refed) WT and *hsf1*$^{-/-}$ mice. Level of NAMPT protein normalized to β-actin loading control relative to WT fed is shown (lower right; n = 4–5 mice per group). (C) Representative Western blot of subcellular NAMPT levels in fed WT and *hsf1*$^{-/-}$ mice (from three experiments). (D) Levels of NAMPT and HSP70 mRNA and protein in hepatocytes from WT and *hsf1*$^{-/-}$ mice in the absence (C) or presence of heat shock (43°C/20 min). Ratio of NAMPT or HSP70 to β-actin is shown (n = 3–6 per group). (E) Levels of Nampt mRNA and protein in primary hepatocytes exposed to varying glucose concentrations (n = 4 per group). (F) ChIP quantitative PCR analysis of HSF1 binding to the putative HSE site of the promoter of *Nampt* in WT primary hepatocytes exposed to varying glucose concentrations. Samples from *hsf1*$^{-/-}$ cells (–/–) were used as a control (n = 4 assays). (G) ChIP quantitative PCR assessing HSF1 binding at the putative HSE containing promoter region of *Nampt* or *Hsp70* in livers of fed, fasted, or refed mice (n = 3 assays). (H) Level of HSF1 protein in nuclear and total lysates from livers of *hsf1*$^{-/-}$ and WT mice under fed, fasted, and refeeding conditions (from three experiments). (I) Levels of NAD⁺, ATP, and glucose output in primary hepatocytes from WT and *hsf1*$^{-/-}$ mice exposed to vehicle (control) or 0.5 mM NAM for 16 h (n = 4 per group). (J) NAD⁺ content in livers of WT and *hsf1*$^{-/-}$ mice 1 h after treatment with 400 mg/kg NAM (i.p.) or vehicle (control; n = 4 mice per group). (K) *Nampt* mRNA in primary hepatocytes transduced with adenovirus carrying GFP or HSF1 overexpression (48 h) and exposed to varying glucose concentrations (n = 6 assays). For all panels, error bars show mean ± SD. *, P < 0.05; **, P < 0.01; ***, P < 0.001. Bars represent WT (red) or *hsf1*$^{-/-}$ (blue) mice.

MFN1) were not affected (Fig. S3 B). However, we noted a significantly higher MFN2 level after prolonged fasting in *hsf1*$^{-/-}$ mice, which may be critical to maintain mitochondrial fusion. Strikingly, *hsf1*$^{-/-}$ mice exhibited a lower p-DRP1/DRP1 ratio under nutrient-available conditions, indicating impaired mitochondrial fission (Fig. S3 B). Tetramethylrhodamine ethyl ester (TMRE) staining indicated that *hsf1* deletion increased the mitochondria potential and conferred mitochondria resistant to carbonyl cyanide *m*-chlorophenyl hydrazone–induced mitochondrial membrane depolarization and cell death. Unexpectedly, we found that HSF1 loss moderately decreased cytoplasmic and mitochondrial reactive oxygen species levels, based on dihydroethidium and MitoSOX staining of primary hepatocytes (unpublished data). This supports the notion that HSF1 loss engages mitochondria fusion to preserve the mitochondrial integrity. Thus, it is conceivable that the altered mitochondrial dynamics in *hsf1*$^{-/-}$ mice represents an adaptive (compensatory) response to reduced NAD^+ and ATP production.

We next assessed the impact on mitochondrial metabolic function under cellular stress. We therefore measured the oxygen consumption rate (OCR), an indicator of mitochondrial OXPHOS, and the extracellular acidification rate (ECAR), an indicator of lactate production and glycolysis. Remarkably, *hsf1*$^{-/-}$ primary hepatocytes presented a low OCR normalized to cell number. Indeed, HSF1 loss markedly decreased both basal and ATP-coupled OCRs and maximal respiratory capacities (Fig. 4 A). However, the overall OCR profile was comparable in both genotypes, when normalized to mitochondrial protein or DNA levels (unpublished data). HSF1 loss also attenuated the OCRs induced by glucose, pyruvate, and lactate, or palmitate, when normalized to cell number (Fig. 4, B–D). In contrast, *hsf1*$^{-/-}$ cells presented an ECAR slightly above WT levels (Fig. 4 E). To directly characterize mitochondrial function, we also examined the respiratory capacity of isolated mitochondria. In the absence of HSF1, the overall mitochondrial respiration capacity was barely affected (Fig. 4 F). Mitochondrial complex I (MC-I) activity was an exception to this pattern, as it was slightly but reproducibly reduced in *hsf1*$^{-/-}$ mitochondria. We confirmed this result using a modified assay for measuring MC-I enzymatic activity (Spinazzi et al., 2012; Fig. 4 G). Blue native (BN) PAGE and Western blot analyses of liver mitochondria lysates for OXPHOS or representative proteins of respiratory chain complexes (C-I to C-V) showed no apparent changes, indicating that except for MC-I activity, the respiratory complex superassemblies were not significantly affected upon HSF1 loss (Fig. 4, H and I). In summary, these results suggest that the impaired respiration and ATP production capacity in *hsf1*$^{-/-}$ cells is likely to be caused by decreased mitochondrial density and, to a lesser extent, by a modest decrease in MC-I–supported respiration as a result of changes in NAD^+/NADH ratio and altered redox state rather than by dysfunctional respiratory complex organization.

To examine whether HSF1 loss might also impair ATP production and OCR through mechanisms affecting nutrient flux and utilization, we measured the steady-state levels of metabolites involved in major bioenergetic pathways. Targeted gas chromatography–mass spectrometry analyses of livers from fed or fasted *hsf1*$^{-/-}$ mice compared with WT controls did not reveal an overt effect in metabolite levels associated with glycolysis, tricarboxylic acid cycle, and lipid metabolism (unpublished data). The potential influence of conversion of pyruvate to lactate or the reverse, which is catalyzed by LDH enzymes and regenerates or consumes NAD^+, is also not supported by our data (unpublished data). Thus, although *hsf1*$^{-/-}$ livers displayed a trend to increased [lactate]/[pyruvate] ratio, cellular lactate concentration did not significantly differ between the genotypes, suggesting that the NAD^+ content deficit is unlikely to be primarily mediated by changes in this redox status. We further conducted stable isotope tracer analysis with [U-^{13}C]-glucose to assess whether glucose metabolism was altered in hepatocytes. Comparable concentrations of ^{13}C-enrichment (fractional abundance of M+2 isotopomers) were observed for the major tricarboxylic acid cycle metabolites between the genotypes (Fig. 4 J). This suggests that HSF1 ablation did not significantly impair the flux of glucose through the tricarboxylic acid cycle and glycolysis in primary hepatocytes.

Effects of HSF1 depletion on NAD^+-dependent sirtuin activation and PGC1α axis regulation

Silencing HSF1 in hepatocytes did not impair ETC formation and respiratory chain capacity as assessed at the mitochondrial protein level. We propose, therefore, a model whereby the effects of HSF1 loss on mitochondrial content can be linked to sirtuin loss of function that leads to increased levels of acetylation of proteins related to organization of the mitochondrial DNA (mtDNA) genome. Among the mammalian sirtuins, nuclear sirtuin 1 (SIRT1) and mitochondrial SIRT3 have robust deacetylase activity. Activated by a rise in NAD^+ level and changes in the NAD^+/NADH ratio, SIRT1 and SIRT3 play a critical role in promoting metabolic adaptations to energy stress by enhancing mitochondrial biogenesis and OXPHOS (Cantó et al., 2015). In light of the established role of PGC-1 isoforms in mitochondrial function and a recent study on the potential role of HSF1 as a transcriptional regulator of PGC-1α in fat and muscle (Ma et al., 2015), we investigated the effects of *hsf1* deletion on hepatic PGC-1α/β expression. *hsf1* deletion significantly reduced the fasting-induced mRNA level of *Pgc-1α* relative to control, although it only had a transient (confined to a 24-h fasting time point) and moderate effect on PGC1α protein levels. The mRNA and protein levels of *Pgc-1β* were not affected (Figs. 3 G and 5 A). In contrast, *hsf1*$^{-/-}$ mice displayed increased protein acetylation of PGC-1α, a known target of SIRT1 (Fig. 5 B). Similar to murine liver, knockdown of HSF1 increased PGC-1α acetylation in human cell lines (HepG2 and 293T; Fig. 5, C and D). Consistent with the finding that PGC-1α activity is inhibited by acetylation, the mRNA levels of PGC-1α target genes (e.g., *Nrf1*, *Nrf2*, and *Cox5*) in response to nutrient deprivation were reduced in *hsf1*$^{-/-}$ mice (Fig. 3 G). As a specific readout of SIRT3 activity loss, we profiled acetylated mitochondrial proteins from *hsf1*$^{-/-}$ and WT liver targets. Acetylation of NDU FS3, MT-CO1, SOD2, and TFAM was increased in *hsf1*$^{-/-}$ livers, whereas NDUFA9, UQCRC2, and ATP5A acetylation was unchanged (Fig. 5 E). These data provide evidence linking HSF1 loss to broad-scale changes in acetylation status of SIRT1 and SIRT3 nuclear and mitochondrial target proteins.

Conceivably, the relative effect of *hsf1* deletion on mitochondrial content might be explained by changes in protein acetylation status accompanied by attenuation of the NAD^+-SIRT1-PGC-1α axis. However, PGC-1α/β seems to be dispensable for mitochondrial density and mtDNA content (Rowe et al., 2013). Interestingly, recent biochemical analyses have provided corroborating evidence that changes in sirtuin activity influence the acetylation and activity of proteins in diverse metabolic path-

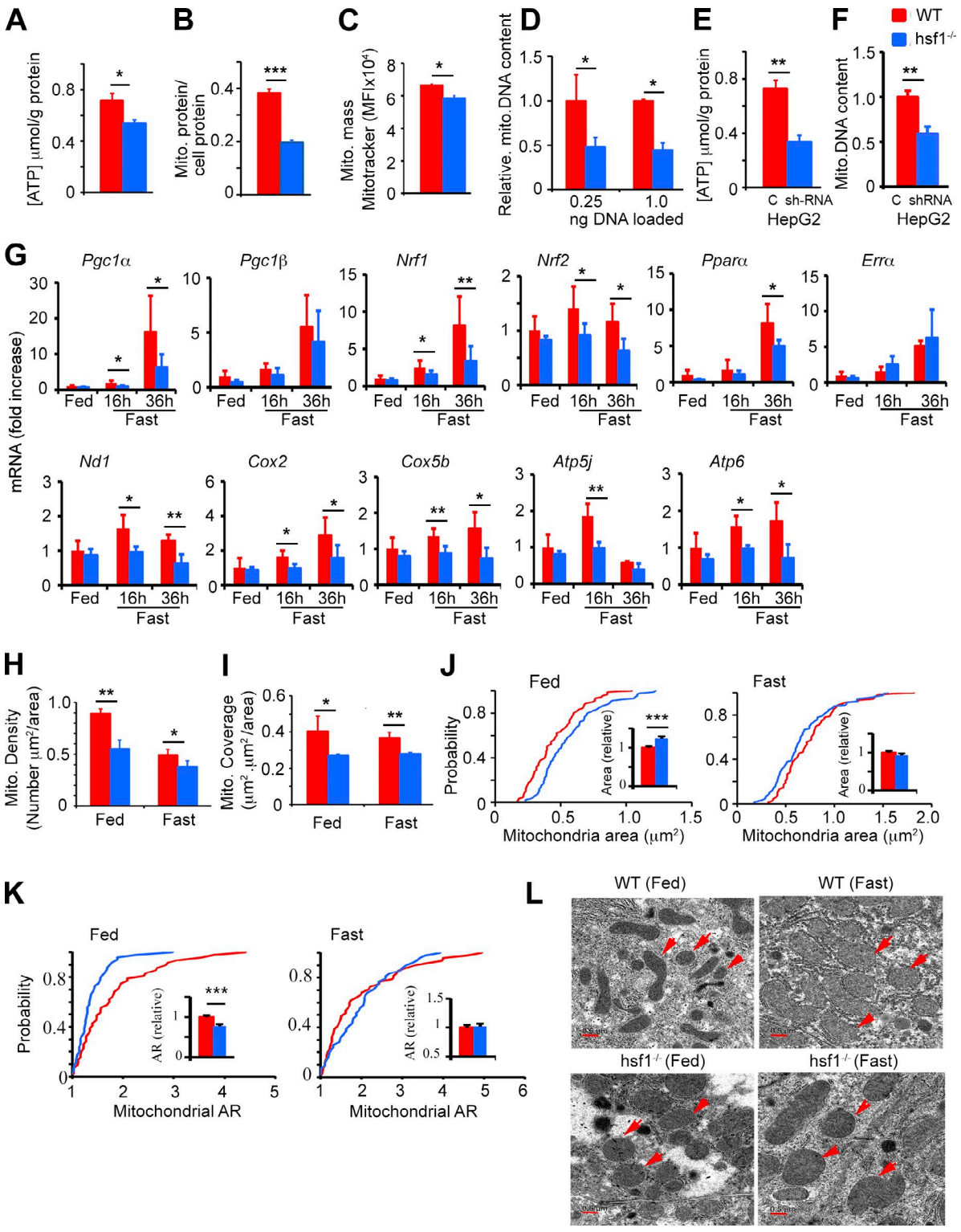

Figure 3. **Effects of *hsf1* deletion on hepatic mitochondrial dynamics and biogenesis.** (A–D) Primary hepatocytes from *hsf1*$^{-/-}$ and WT mice were cultured overnight and assayed for ATP content (A), mitochondria protein content (B), mitochondria mass by monitoring mean fluorescence intensity (MFI) of MitoTracker Deep Red by flow cytometry (C), and mtDNA content (D), determined by quantitative PCR and expressed as the amount of mtDNA (*Cytb*) relative to nuclear DNA (*βactin*). (E and F) ATP and mtDNA content of HepG2 cells with intact or loss of HSF1 by shRNA knockdown ($n = 4–6$ cell samples per group in A–F). (G) Relative mRNA levels of genes associated with mitochondrial biogenesis in the livers of fed or fasted (fast) *hsf1*$^{-/-}$ mice and WT controls ($n = 5$ mice per group). (H–L) EM images and quantification of mitochondrial shape and morphology in livers of fed or 36-h fasted WT and *hsf1*$^{-/-}$ mice showing mitochondria density (H), mitochondria coverage (I), and cumulative probability distribution of cross-sectional mitochondria areas (J) and mitochondrial AR (K). Insets show relative changes in mean mitochondria area and AR between genotypes. Data analyses were based on evaluation of mitochondria in 60 randomly selected microscopic fields of three mice per group. Bars in inserts show mean ± SD. (L) Representative EM images of mitochondria in liver sections from fed or 36-h fasted mice. Red arrows indicate mitochondria. Bars, 0.5 µm. For all panels, error bars show mean ± SD. *, $P < 0.05$; **, $P < 0.01$; ***, $P < 0.001$. Bars represent WT (red) or *hsf1*$^{-/-}$ (blue) mice.

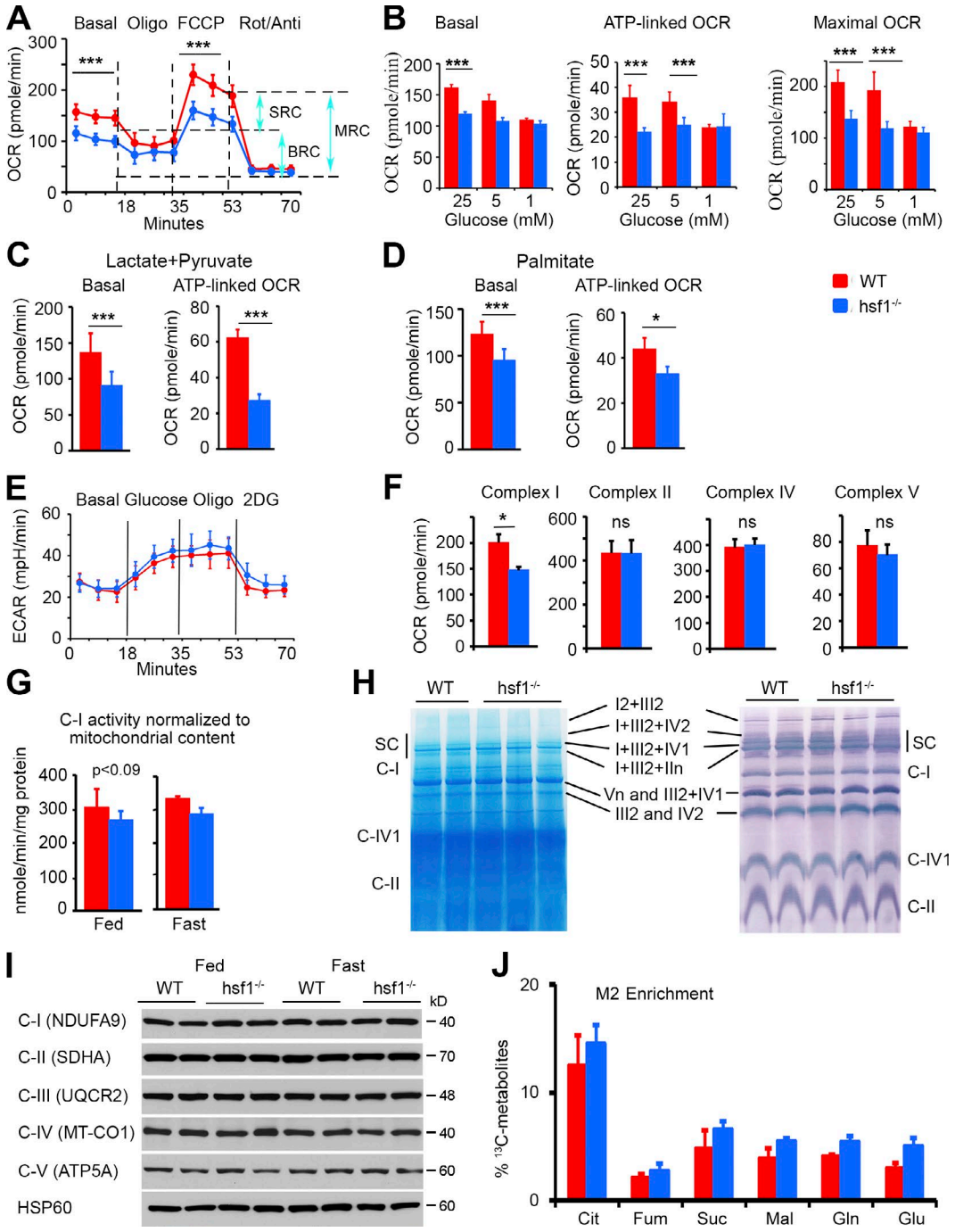

Figure 4. **HSF1 deletion impairs mitochondria respiratory capacity.** (A–E) OCR and ECAR measured in primary hepatocytes from WT or *hsf1*$^{-/-}$ mice. Notably, oligomycin (Oligo) inhibits ATP synthesis, FCCP uncouples OXPHOS, rotenone (Rot) inhibits mitochondrial complex I (C-I), and antimycin A (AA) inhibits C-III in the respiratory chain. (A) OCR profile normalized to cell number. SRC, spare respiratory capacity; MRC, maximal respiratory capacity; BRC, basal respiratory capacity. (B–D) Basal, ATP-linked, and maximal OCR values in hepatocytes fed with indicated concentrations of glucose (B), 10 mM lactate + 1 mM pyruvate (C), or 1 mM palmitate for 2 h (D). (E) ECAR profiles. Glycolytic reserves (mobilized with oligomycin and inhibited with 2-deoxy-glucose [2DG], respectively) were measured using a Seahorse XF96 Analyzer. Vertical lines denote injection of individual compounds (n = 3 experiments in A–E). (F) Respiration of liver mitochondria from 24-h fasted WT and *hsf1*$^{-/-}$ mice. Assessment of complex I (C-I) II, IV and V respiration based on data from mitochondrial coupling assays. Bars are mean ± SD (n = 3–5 replicate wells per analysis in at least 2 experiments). (G) C-I–specific activity in mitochondrial liver extracts from fed or fasted mice, normalized to mitochondria protein (n = 3 mice per group). (H) Representative BN-PAGE performed with isolated mitochondria from fed WT and *hsf1*$^{-/-}$ livers and demonstrating normal distribution of MCs and assembly of supercomplexes (SCs). After electrophoresis, gels were processed for Coomassie blue G250 staining or immunoblotting with an OXPHOS antibody cocktail (at least three experiments). (I) Western blot analysis of representative proteins for ETC complexes (I–V) in liver mitochondrial extracts of fed or 16-h fasted mice indicating no significant differences between the genotypes (three experiments). (J) Mass isotopomer (m + 2) distribution analysis of indicated tricarboxylic acid cycle metabolites in primary hepatocytes from WT and *hsf1*$^{-/-}$ mice. Cells were incubated with 20mM [U-6-^{13}C]-glucose for 6 h. Metabolites were profiled by gas chromatography–mass spectrometry and normalized to cell number. (n = 4 mice per group). For all panels, error bars show mean ± SD. *, P < 0.05; ***, P < 0.001; ns, not significant. Bars represent WT (red) or *hsf1*$^{-/-}$ (blue) mice.

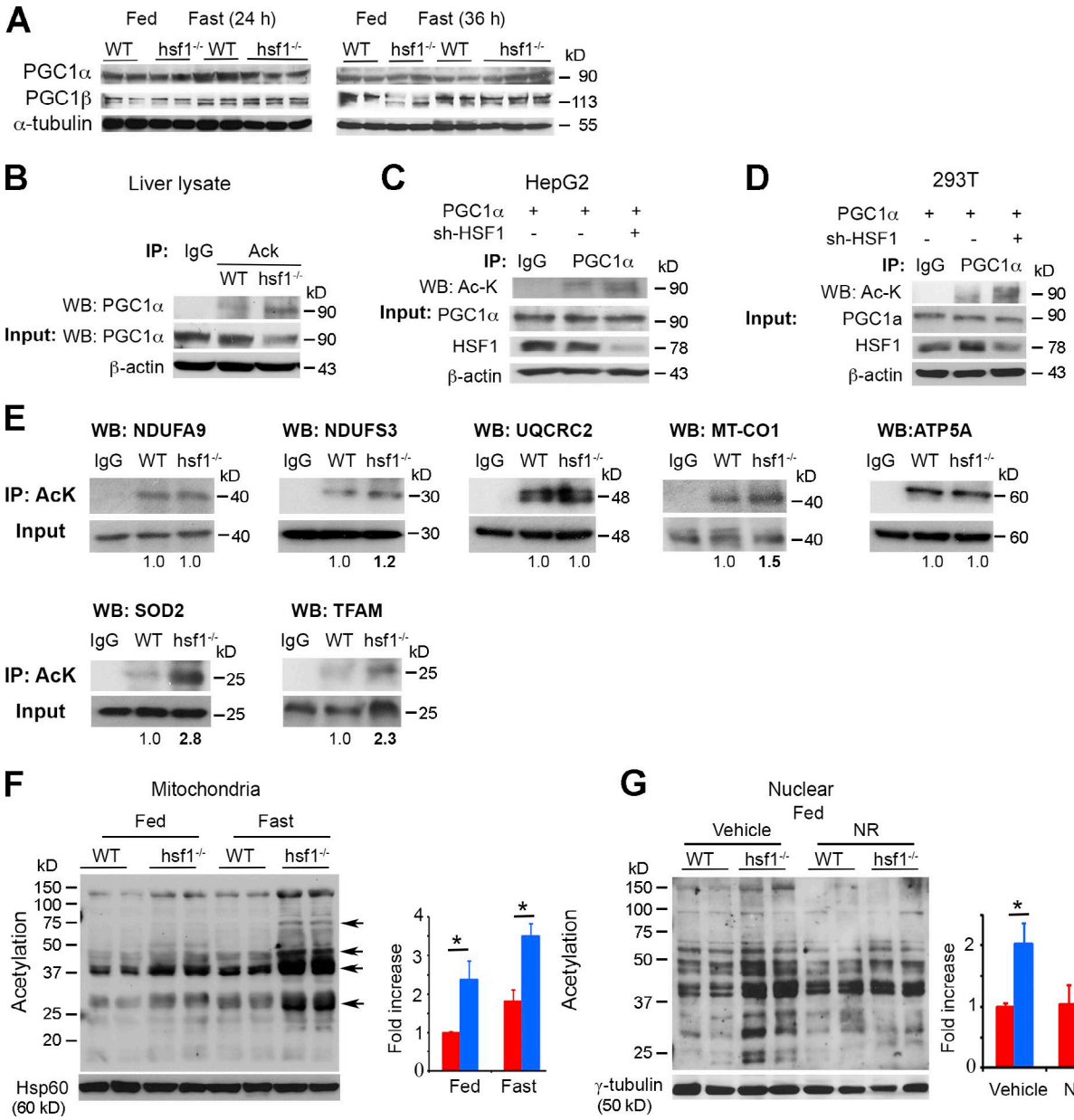

Figure 5. **HSF1 ablation affects protein acetylation via SIRT1 and SIRT3.** (A) Nutrient-induced protein levels of PGC-1α/β in livers of fed or fasted WT and *hsf1*$^{-/-}$ mice (n = 4 from two experiments). (B–D) Increased acetylated PGC-1α protein level in liver extracts from fed WT and *hsf1*$^{-/-}$ mice (B) and cell lines (C and D). Acetylated proteins were immunoprecipitated (IP) with an anti–acetylated lysine (Ac-K; B) or PGC-1α (C and D) antibody and analyzed by Western blotting with antibody to PGC-1α or Ac-K. HepG2 or 293T cells were transfected with PGC-1α expression plasmid and treated with sh-HSF1 as indicated (three experiments). (E) Acetylation profiles of SIRT3 target proteins. Mitochondrial liver extracts from fasted WT and *hsf1*$^{-/-}$ mice were immunoprecipitated with an anti–Ac-K antibody and blotted for indicated proteins (three experiments). WB, Western blot. (F) Representative Western blot for Ac-K residues in isolated mitochondria extracts from livers of WT and *hsf1*$^{-/-}$ mice during fed or 24-h fasting states. The arrows identify potential sirtuin target proteins that change the acetylation level. Quantification of Ac-K proteins (normalized by fed WT mice) is shown (n = 5 mice per group). (G) A representative Western blot for Ac-K residues in nuclear extracts from livers of WT and hsf1$^{-/-}$ mice treated with vehicle (control) or 400 mg/kg NR daily for 7 d. Quantification of Ac-K proteins (normalized by vehicle-treated WT mice) is shown (right; n = 5 mice per group). For all panels, error bars show mean ± SD. *, P < 0.05; **, P < 0.01; ***, P < 0.001. Bars represent WT (red) or hsf1$^{-/-}$ (blue) mice.

ways, including those regulating mitochondrial content integrity and genome maintenance (Hebert et al., 2013). We first profiled the mRNA expression of genes associated with the basal transcription machinery of mitochondria. Fasting-induced mRNA levels of genes involved in mtDNA replication were reduced in *hsf1*$^{-/-}$ livers (Fig. S3 C), which is consistent with the observed marked decreased in mtDNA content. We next explored, biochemically, whether the specific mitochondrial adaptive pathways are modified by *hsf1* deletion. Sirtuin-dependent mitochondrial changes associated with decreased mtDNA content are linked to induction of the mitochondrial unfolded protein response (UPR^{mit}), which is triggered by an imbalance in mitochondrial- versus nuclear-encoded mitochondrial proteins (Mouchiroud et al., 2013). However, no differences in mitonuclear protein ratio (SDHA/MT-CO1; Fig. S3D), mRNA expression of UPR^{mit} (*Clpp*, *Hspe1*, or *Hspd1*; Fig. S3E), or UPR^{ER}

(GRP78, XPB1, and ATF4) protein biomarkers (Fig. S3 F) were detected between the genotypes.

Finally, we sought to alter the protein acetylation status by manipulating the cellular NAD^+ level in vivo. Consistent with the notion that the activity of sirtuins (including SIRT1 and SIRT3) is inhibited by a lower NAD^+ level or NAD^+/NADH ratio, we found that nuclear and mitochondrial extracts from livers of *hsf1*$^{-/-}$ mice exhibited increased protein acetylation (Fig. 5, F and G). Interestingly, the increased protein acetylation status of mitochondria isolated from *hsf1*$^{-/-}$ livers could be reversed by treatment of mice with NR, which increases the NAD^+ level and normalizes the NAD^+/NADH ratio (Fig. 5 G). Importantly, the NR supplementation in *hsf1*$^{-/-}$ mice increased mitochondrial mass and DNA abundance in hepatic cells (unpublished data). Collectively, these findings established links among HSF1, the NAD^+/NADH ratio, and protein acetylation status largely regulated by SIRT1 and SIRT3, connecting mitochondrial biogenesis to respiratory function and ATP production.

HSF1 depletion inhibits ATP-consuming biosynthetic pathways

The idea that cells must successfully balance metabolic demands with energetic requirements to maintain viability prompted us to investigate potential effects of *hsf1* deletion on nutrient and energy-regulated anabolic pathways, including gluconeogenesis, protein translation, and lipid metabolism.

Hepatic glucose production is central to metabolic adaptation during fasting and occurs most efficiently with substrates generated by catabolism of glycogen, glycerol, or lactate/pyruvate/amino acids. In this process, mitochondria play a pivotal role through provision of carbon substrates, reducing equivalents, and ATP. Consistent with our previous study (Jin et al., 2011), we found that *hsf1*$^{-/-}$ or L-*hsf1*$^{-/-}$ mice exhibited a markedly improved glucose tolerance and displayed lower blood glucose levels after pyruvate or glucagon exposure (Fig. 6, A and B). Basal blood glucose levels during the fed or fasting states were reproducibly lower in both *hsf1*$^{-/-}$ and L-*hsf1*$^{-/-}$ mice than in WT controls (Fig. 6, C and D). These data suggest that HSF1 is required for proper regulation of glucose signals. Indeed, insulin stimulation of p-AKT, which reflects its activation, was significantly enhanced in the absence of HSF1 (Fig. 6 E). Increased AKT signaling by insulin was also evident in primary L-*hsf1*$^{-/-}$ and *hsf1*$^{-/-}$ hepatocytes (unpublished data). Next, we determined whether HSF1 ablation exerts its effects by inhibiting hepatic gluconeogenesis mediated by glucagon signaling (Miller et al., 2013). Binding of glucagon to its receptor on the hepatocyte plasma membrane leads to activation of adenylyl cyclase, production of cAMP, and stimulation of protein kinase A (PKA), which phosphorylates protein targets that work in concert to increase hepatic glucose output (Oh et al., 2013). Consistent with an effect on gluconeogenesis, primary *hsf1*$^{-/-}$ hepatocytes produced significantly less glucose when stimulated with lactate and pyruvate, glucagon, or forskolin (FSK), but this inhibitory effect is reversed by an analogue of cAMP (Bt2-cAMP; Fig. 6 F). Interestingly, HSF1 loss did not affect glucagon receptor expression, but caused significant reductions in the glucagon- or FSK-stimulated increase in cAMP levels (Fig. 6, G and H). The decreased glucose production capacity paralleled attenuation of glucagon or FSK-induced signaling that was associated with reduced phosphorylation of PKA substrates; this inhibition was bypassed by Bt2-cAMP (Fig. 6 I). Specifically, *hsf1* deletion reduced expression levels of glucagon or FSK-induced p-CREB or nuclear active dephosphorylated CRTC2 (TORC2), which are PKA-regulated proteins, as well as reduced mRNA levels of key gluconeogenic genes (Fig. 6, J and K); as expected Bt2-cAMP-dependent signaling induction was not affected (Fig. 6 L). To further dissect the mechanism of blunted glucagon action, glucagon-stimulated signals were assessed. Fasting or injection of glucagon stimulated hepatic p-CREB in WT mice, but this expression was significantly reduced in *hsf1*$^{-/-}$ and L-*hsf1*$^{-/-}$ livers (Fig. S4, A–F). In line with a previous study (Jin et al., 2011), *hsf1*$^{-/-}$ mice also displayed increased AKT-FOXO1 signaling not only upon feeding, which stimulates insulin production, but also upon fasting when the insulin level is low. Interestingly, the combined significant increase in acetylated-FOXO1 and p-FOXO1 levels seen in the livers of *hsf1*$^{-/-}$ mice upon fasting caused a more pronounced hepatic nuclear exclusion and inhibition of FOXO1 activity during gluconeogenesis (Fig. S4 G), which is consistent with a recent study (Qiang et al., 2010).

Remarkably, in spite of the increased nutrient-stimulated AKT-mediated signals caused by HSF1 ablation, a marked decrease in the activities of mTOR and its downstream target proteins (p70S6K, S6R, and 4E-BP), which stimulate mitochondrial biogenesis and protein translation (Morita et al., 2013), was evident (Fig. 7 A). This effect, which can be explained by the concomitant ATP decline combined with a powerful increase in hepatic AMPK activity, caused a significant decrease in global translation relative to control as measured by ^{3}H-Leu labeling in primary hepatocytes or polysome profiling performed on liver extracts from fed or fasted *hsf1*$^{-/-}$ mice (Fig. 7, B and C). These in vitro and in vivo findings further support the conclusion that HSF1 activity and hepatic metabolic activity may be integrated with nutritional state and protein translation.

In cells, most metabolic pathways contain multiple levels of feedback control to maintain cellular ATP. Fatty acid oxidation (FAO) intertwined with the tricarboxylic acid cycle and ETC activity is a major supplier of ATP during fasting. This prompted examination as to whether the decreased hepatic ATP production in the absence of HSF1 is linked to changes in hepatic FAO or lipid synthesis. We observed no changes in basal FAO during the fed state but a slightly lower FAO level during the fasting state in the *hsf1*$^{-/-}$ livers (Fig. 7 D). However, liver cells from *hsf1*$^{-/-}$ mice exhibited significantly reduced lipid production (Fig. 7 E).

Collectively, these data confirmed that the hepatic energy deficit caused by HSF1 loss triggers compensatory pathways to restore intracellular energy levels through inhibition of ATP-consuming biosynthetic pathways. Moreover, our data suggest that these effects are likely due, at least in part, to the effects of AMPK activation and lower ATP levels.

NAD precursors reverse the NAD^+ deficit caused by HSF1 inactivation and improve hepatic metabolic capacity

Several pharmacological and genetic approaches have been explored to increase NAD^+ bioavailability and enhance sirtuin activity as a strategy to ameliorate and protect organisms from metabolic diseases induced by excessive nutrient consumption, aging, or genetic disorders (Cantó et al., 2015). The ability of NAD precursors to increase NAD^+ levels in vivo and in vitro (Yoshino et al., 2011; Cantó et al., 2012) prompted us to test whether the reduced NAD^+ levels in *hsf1*$^{-/-}$ hepatic cells can be reversed by NAD^+ precursors. Indeed, supplementation with

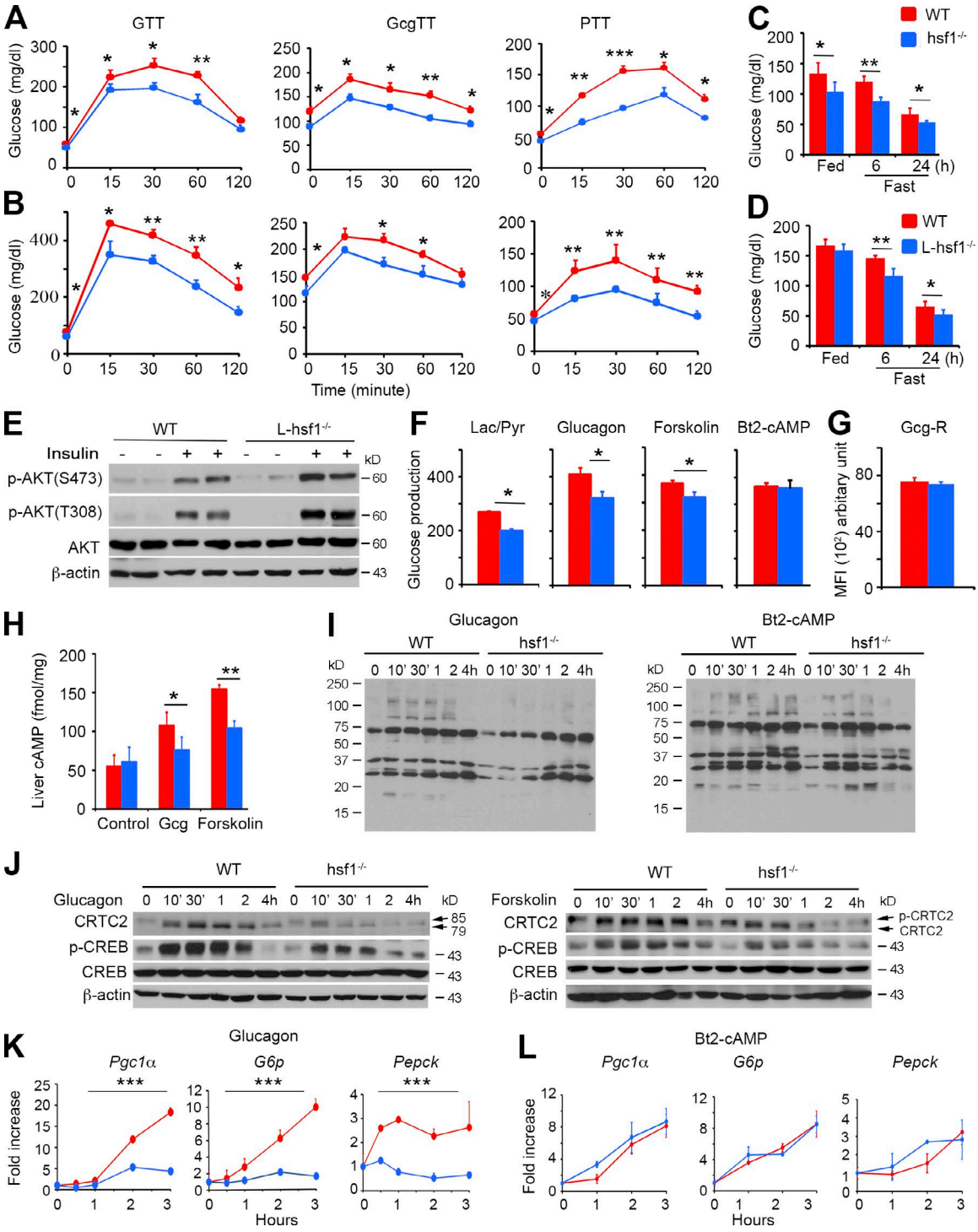

Figure 6. **HSF1 ablation inhibits glucagon signaling and glucose production in liver.** (A and B) Results of glucose, pyruvate, and glucagon (Gcg) tolerance tests (GTT, PTT, and GgcTT) in WT versus *hsf1*$^{-/-}$ mice (A) or WT versus L-*hsf1*$^{-/-}$ mice (B) are shown. (C and D) Fed or fasting glucose levels in WT, *hsf1*$^{-/-}$, or L-*hsf1*$^{-/-}$ mice. (E) Western blot analyses for p-AKT in livers of L-*hsf1*$^{-/-}$ mice compared with WT controls. Liver extracts were prepared 10 min after i.p. injection of 0.75 mU/g insulin. (F) Glucose output in primary hepatocytes from WT and *hsf1*$^{-/-}$ mice exposed to pyruvate and lactate, glucagon, FSK, or Bt2-cAMP for 4 h. Glucose levels were determined in the medium. (G) Expression of glucagon receptor (Gcg-R) in primary hepatocytes by antibody staining and FACS analysis. Values are expressed as mean fluorescence intensity (MFI). (H) 4-h fasted primary hepatocytes from WT or *hsf1*$^{-/-}$ mice, were treated with 100 nM glucagon or 10 µM FSK for 15 min, lysed and assayed for total cellular cAMP. (I) Primary hepatocytes from WT or *hsf1*$^{-/-}$ mice starved for 4 h were treated with 100 nM glucagon or 100 µM Bt2-cAMP for the indicated times and analyzed by Western blotting with p-PKA substrate antibody. A representative blot from three analyses is shown. X', minutes. (J) Glucagon- or FSK-stimulated p-CREB and CRTC2 expression in primary hepatocytes from WT or *hsf1*$^{-/-}$ mice. Cells were treated as in I and analyzed by Western blotting with the indicated antibodies. (K and L) Relative glucagon- or Bt2-cAMP-induced mRNA levels of gluconeogenesis genes in primary hepatocytes from WT or *hsf1*$^{-/-}$ mice treated as in panel I and assayed at the indicated times. For all panels, error bars show mean ± SD. *, $P < 0.05$; **, $P < 0.01$; ***, $P < 0.001$. Bars indicate WT (red) or *hsf1*$^{-/-}$ (blue) mice (n = 4–6 mice per group in A–E; data in F–H, K, and L are from triplicate wells and repeated at least twice; four experiments in J).

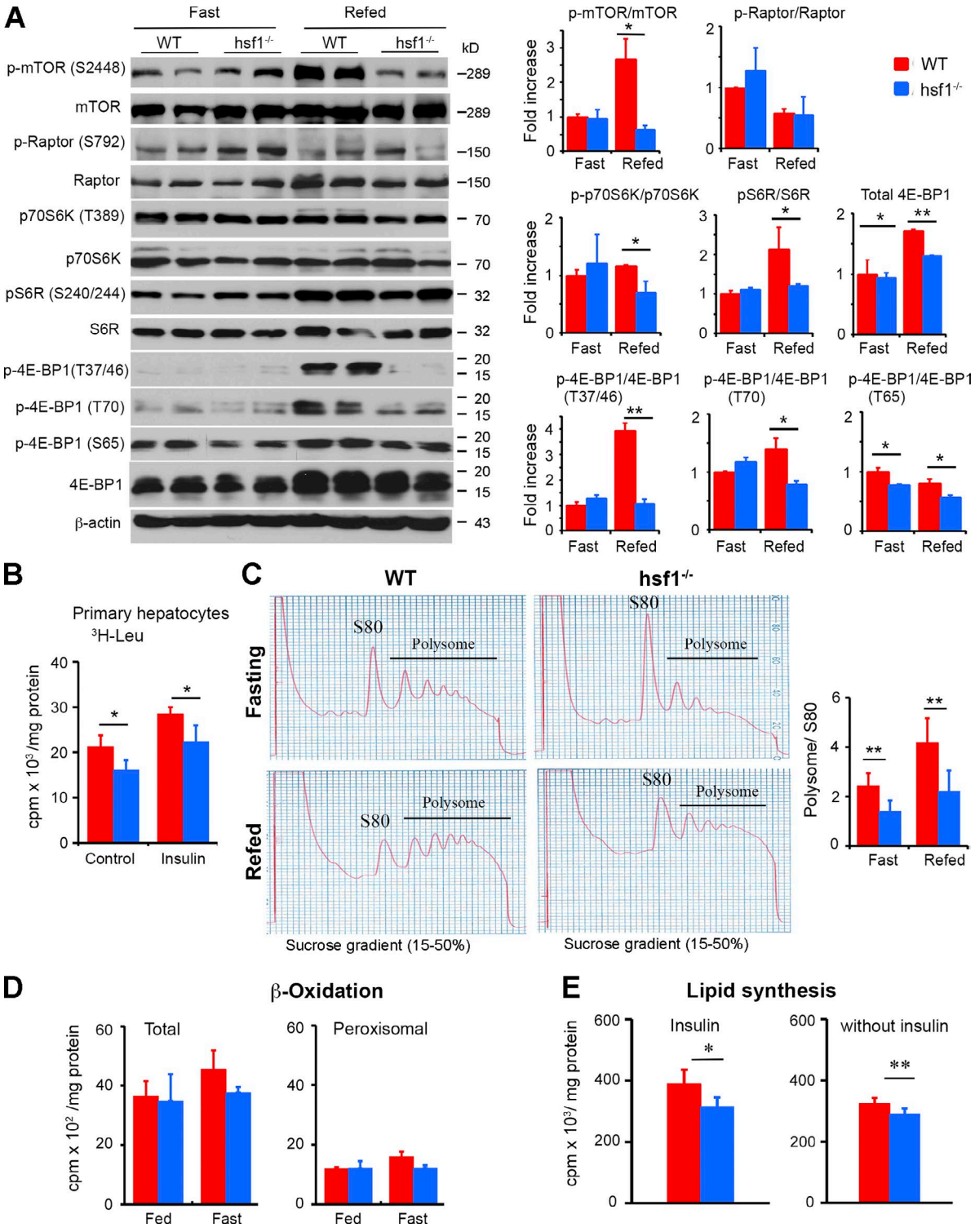

Figure 7. ***Hsf1* deficiency suppresses hepatic protein translation and lipid synthesis.** (A) Nutrient-induced mTOR-signaling. Western blot analysis and quantification of the indicated proteins in liver samples from 24-h fasted or 3-h refed WT and *hsf1*$^{-/-}$ mice. Blots were quantified by densitometry (right). Level of phosphorylated proteins normalized to total level was expressed as relative fold increase to control (WT, fasted) that was arbitrarily set at 1 (100%). Bars are mean ± SD (n = 5 mice per group). (B) Protein synthesis rates in primary hepatocytes from WT and *hsf1*$^{-/-}$ mice. ^{3}H-Leu labeling experiments in isolated cells stimulated with 100 nM insulin for 30 min or vehicle and pulsed with ^{3}H-Leuc for 30-min ^{3}H incorporation into soluble cellular protein was qualified and normalized to the total protein. (C) Polysomal profiles from livers of WT and *hsf1*$^{-/-}$ mice. For quantification, the area under the curve was calculated for 80S peaks and polysomal peaks. Representative polysome profiles for 24-h fasted or 3-h refed mice and the ratio of polysome to 80S are shown (right). Error bars in B and C represent mean ± SD; experiments were performed in triplicate and repeated at least twice. (D) Fatty acid β oxidation in fresh livers derived from WT controls and *hsf1*$^{-/-}$ mice under fed or 24-h fasted conditions. Error bars represent mean ± SD; (n = 4 mice per group). (E) De novo lipogenesis activity in the primary hepatocytes from WT and *hsf1*$^{-/-}$ mice, stimulated with 100 nM insulin (4 h) or vehicle (n = 4 mice per group). For all panels, bars indicate WT (red) or *hsf1*$^{-/-}$ (blue) mice. Statistical significance is indicated (*, $P < 0.05$; **, $P < 0.01$).

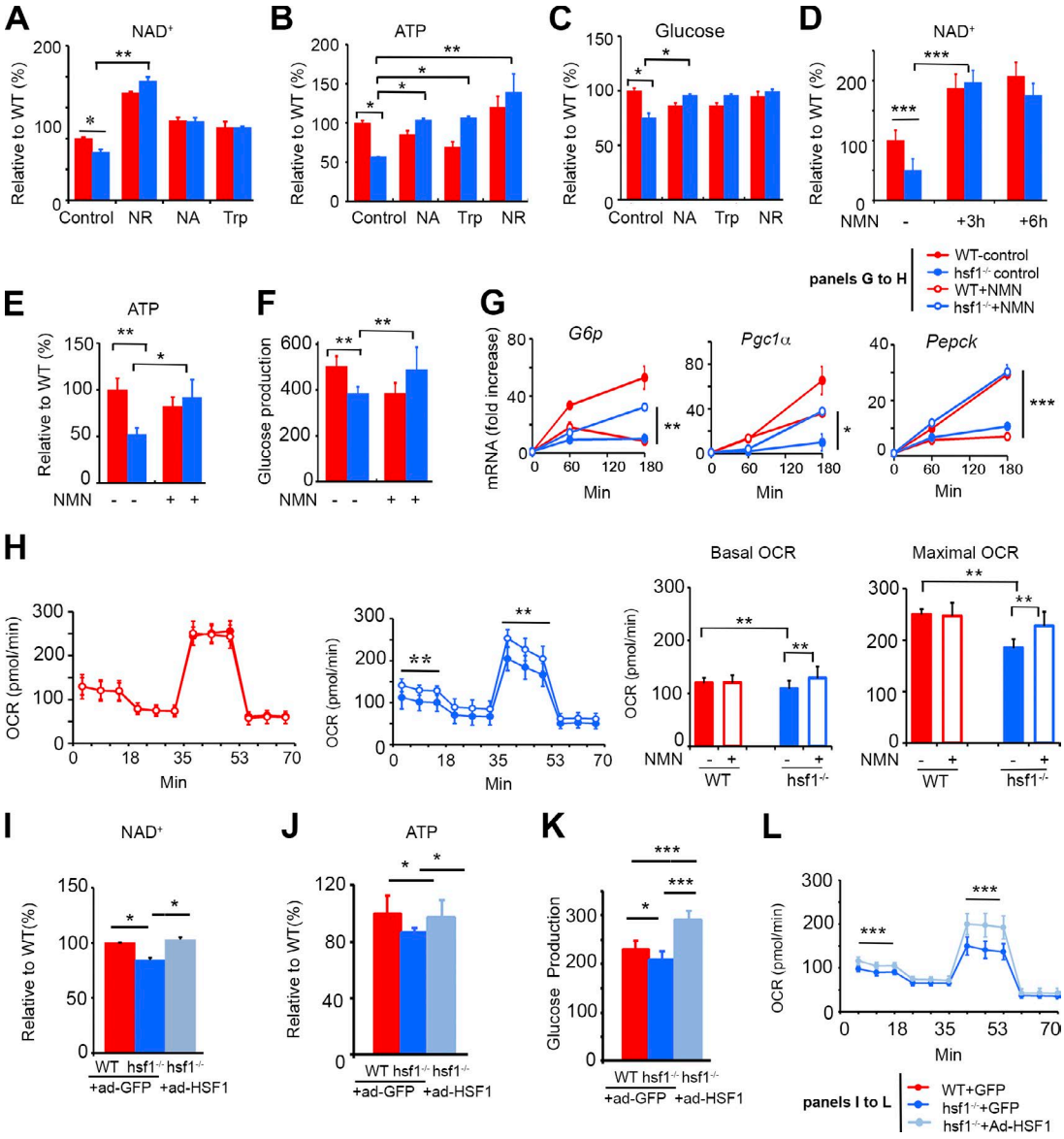

Figure 8. **Supplementation with NAD+ precursors ameliorates the hepatic bioenergetics deficit caused by HSF1 loss.** (A–C) Levels of NAD+ (A) and ATP (B) and glucose output (C) in primary hepatocytes from WT and *hsf1*$^{-/-}$ mice exposed to vehicle (control) or NAD+ precursors (0.5 mM NA, NR, or TRP) for 16 h. (D–F) Primary hepatocytes from WT and *hsf1*$^{-/-}$ mice were treated with vehicle or 0.5 mM NMN for 3 or 6 h, and levels of NAD+ and ATP and glucose output in the medium were determined. (G) Primary hepatocytes from WT and *hsf1*$^{-/-}$ mice were treated with vehicle or 0.5 mM NMN for 16 h and then exposed to 100 nM glucagon for 1 or 3 h. mRNA levels of gluconeogenic genes after glucagon treatment is shown. (H) Representative OCR profiles in primary hepatocytes from WT and *hsf1*$^{-/-}$ mice treated with vehicle or 0.5 mM NMN for 16 h. Bar graphs quantify basal and maximal OCR (right; $n = 9$ from three experiments). (I–L) NAD+, ATP, glucose output and OCR profiles in primary hepatocytes transduced with adenovirus carrying GFP (ad-GFP; control) or HSF1 overexpression (ad-HSF1) for 48 h ($n = 4$ from two experiments). For all panels, error bars show mean ± SD. *, $P < 0.05$; **, $P < 0.01$; ***, $P < 0.001$. Bars in A–F indicate WT (red) or *hsf1*$^{-/-}$ (blue) mice. $n = 6$ (A–G).

NA, NR, or TRP raised the NAD+ and ATP levels and restored glucose production capacity in *hsf1*$^{-/-}$ hepatocytes (Fig. 8, A–C). Likewise, NMN increased NAD+ and ATP levels and improved impaired glucagon-induced mRNA levels of gluconeogenic genes and glucose output (Fig. 8, D–G). In contrast, WT hepatocytes treated with NMN displayed a slight but reproducible decrease in ATP and glucose production levels as well as a marked repression of gluconeogenic genes (Fig. 8, E–G). Consistent with these findings, we found that NMN ameliorated the metabolic dysfunction of mitochondria in *hsf1*$^{-/-}$ hepatocytes, increasing the basal, ATP-linked, and maximal OCRs (Fig. 8 H). Importantly, the effects on NAD+, ATP, glucose, and OCR values could effectively be reversed by overexpression of HSF1 (Fig. 8, I–L). These observations suggest that the energetic defects caused by HSF1 loss sensitize livers and possibly other tissues to NAD precursors and activators of mitochondrial bioenergetics.

Based on these findings, we predicted that the metabolic defects in HSF1-mediated NAD+ biosynthesis could be ameliorated by administration of NR in mice. We observed enhanced NAD+ levels at both the fed and fasting states in NR-treated mice (Fig. 9 A). NR treatment also improved the mtDNA content in *hsf1*$^{-/-}$ mice (unpublished data). In concordance with previous studies (Yoshino et al., 2011; Cantó et al., 2012;

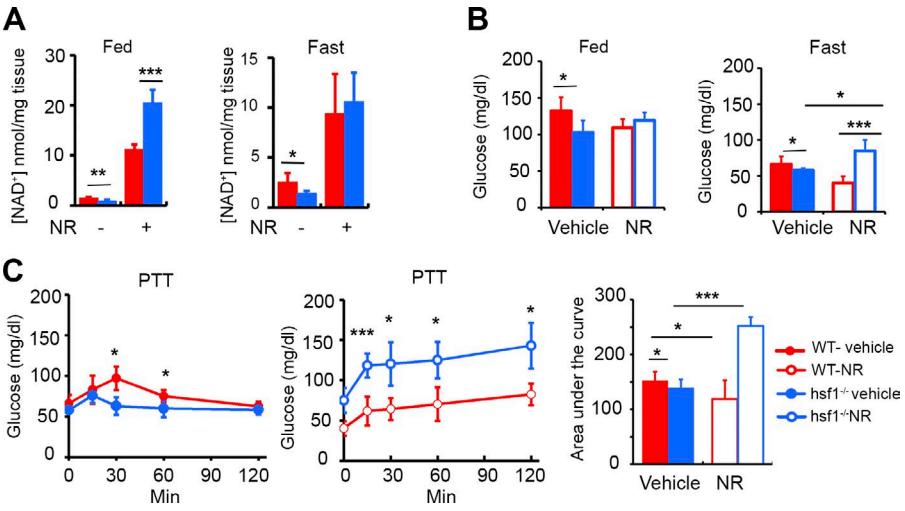

Figure 9. **NR reverses gluconeogenesis and bioenergetic deficits in *hsf1*$^{-/-}$ mice.** (A and B) Fed and 24-h fasting intracellular NAD$^+$ (A) and blood glucose (B) levels monitored in WT or hsf1$^{-/-}$ mice after treatment with vehicle (control) or 400 mg/kg NR daily for 7 d (n = 5 mice per group). (C) PTT in WT or *hsf1*$^{-/-}$ mice after treatment with NR as described in A. The right panel shows the area under the curve of the PTT (n = 5 mice per group). For all panels, error bars show mean ± SD. *, P < 0.05; **, P < 0.01; ***, P < 0.001. Bars indicate WT (red) or *hsf1*$^{-/-}$ (blue) mice. n = 6 (A–G).

Trammell et al., 2016), NR-treated WT mice displayed a lower blood glucose level in both the fed and fasted states (Fig. 9 B). Conversely, by comparing NR with vehicle-treated *hsf1*$^{-/-}$ mice, we found that NR slightly increased glucose levels in the fed state but considerably increased glucose levels in the fasting (Fig. 9 B). Consistent with this result, NR-treated WT mice displayed lower blood glucose concentrations in pyruvate tolerance test (PTT), confirming significantly lower gluconeogenic conversion of pyruvate to glucose (Fig. 9 C). In contrast, NR treatment of *hsf1*$^{-/-}$ mice manifested an increase in PTT, confirming restoration of hepatic gluconeogenesis. The contrasting results of NR treatment on glucose production in WT versus *hsf1*$^{-/-}$ mice prompt speculation that the effects of NAD-precursor supplementation might stem from its ability to cause differential changes in NAD$^+$/NADH ratios that would affect the ATP pools. One would also suspect that the effects of acute NR administration, particularly those on the physiological function of nuclear and mitochondrial sirtuins and their multiple targets, might not be the same between genotypes. Therefore, the detailed molecular mechanisms responsible for this effect need to be investigated further.

Discussion

A common notion holds that the level of ATP is universally homeostatic and, therefore, it is unlikely to be the growth-limiting resource for most cell types (Hochachka and McClelland, 1997; Lunt and Vander Heiden, 2011). Although this may be the case in steady-state conditions, it may not be sufficient for extensive energy-demanding processes. For instance, in several cancer models, the NAD$^+$/NADH and NADP$^+$/NADPH redox function coupled to ATP production levels plays a significant role in dictating survival or death of the tumor cells (Zong et al., 2016). Considering the strong evidence directly linking NAD$^+$/NADH redox imbalance and ATP insufficiency to diverse human pathologies (Verdin, 2015), a key challenge in deciphering metabolic adaptation is the identification of the regulators that maintain cellular energetic efficiency. HSF1 is a central transcriptional regulator of eukaryotic protein quality control, and evidence suggests that it plays a role as a metabolic sensor. Although HSF1 exerts an impact on a large array of cellular functions that are altered during nutrient fluctuation, particularly in malignancy, including translation, ribosome biogenesis, and glucose metabolism (Hahn et al., 2004), the specific mechanisms by which HSF1 may preserve optimal cell function, especially under challenging nutrient and energy-deprived conditions, are not well understood. Here, we validated a mechanism whereby HSF1 monitors the metabolic and bioenergetics and protein synthesis pathways in the cell, acting as a pivotal determinant of key NAD$^+$- and ATP-dependent metabolic hepatic functions during different nutrient states. Although diminished redox function and mitochondrial ATP production capacity are considered sources of impaired cellular function and pathology, surprisingly, HSF1 loss increases cellular fitness and preserves cell viability by triggering an adaptive compensatory response to balance the energy deficit, a response that stems from attenuation of nutrient-regulated anabolic metabolic processes in the liver.

In principle, changes in cellular NAD$^+$ content after depletion of HSF1 could stem from perturbations in cellular reductive capacity (NAD$^+$/NADH ratio), the rate of NAD$^+$ synthesis, and NAD$^+$ consumption. Although our findings support the direct HSF1-mediated control of stress-induced NAMPT expression, perturbation in NAD$^+$ recycling from NADH, a process primarily dependent on MC-I of ETC activity, potentially may contribute to a greater effect on cellular NAD$^+$ deficit. The data also provide strong evidence linking perturbations in the HSF1–NAD$^+$ axis to changes in sirtuin deacetylase activity, global protein acetylation, and hepatic ATP regenerative capacity (Fig. S5). An important question deserving of further investigation is how a widespread upward shift in protein acetylation impacts ATP production capacity, especially considering the contrasting effects of hyperacetylation on protein function (Nogueiras et al., 2012). Several studies linking heightened protein acetylation to metabolic dysregulation posit that at least some of these acetyl modifications alter the activity, mostly in a negative direction, of proteins required to maintain mitochondrial integrity (Hebert et al., 2013). Fitting with this prediction, the effects of HSF1 loss on mitochondrial content could simply be explained by loss-of-function acetylation of proteins that regulate mitochondrial biogenesis, including PGC-1α or TFAM, proteins playing a role in maintenance, expression, and organization of the mitochondrial DNA genome. Although the findings do not prove causation, the aforementioned conclusion is supported by restoration of the NAD$^+$/NADH ratio by NAD precursors reducing protein acetylation and correcting the *hsf1*$^{-/-}$ metabolic phenotype. Also noteworthy is that although NAD$^+$ is a main

substrate for class III (sirtuin) deacetylase activity, changes in the NAD^+/NADH ratio have also been shown to modulate sirtuin activity (Karamanlidis et al., 2013). Competitive inhibition of sirtuin activity by a lower NAD^+/NADH ratio thus might further stimulate protein acetylation.

Mitochondrial dynamics (fusion and fission) hold a prominent position in mtDNA stability, respiratory capacity, response to nutrient availability, and mitophagy. For example, defective mitophagy caused by excessive cleavage of PINK1 represents a feature of DNA repair disorders (Fang et al., 2014). Thus, in theory, the mitochondrial phenotype of *hsf1*$^{-/-}$ mice was predicted to involve increased mitophagic elimination of altered mitochondria. However, our findings of intact autophagy and inability of mitochondria to engage fission in livers of *hsf1*$^{-/-}$ mice did not support this notion. As HSF1 has no discernible adverse effects on cell viability, these data predict that the energetic performance of stressed mitochondria in *hsf1*$^{-/-}$ mice will be retained through fusion reactions that maximize the energy output rather undergo mitophagy.

Based on this information, we propose a model (Fig. S5) whereby loss of HSF1 triggers an energy-saving adaptive response associated with inhibition of nutrient-driven hepatic anabolic metabolic processes. Preservation of fasting energetics through attenuation of gluconeogenesis, an energetically costly anabolic process requiring six ATP equivalents per molecule of glucose synthesized, is likely to be an important mechanism to counteract systemic hyperglycemia, for example, in diabetic patients. This process is regulated by a set of well-described signaling pathways, including the glucagon–PKA–CREB and CRTC2 axis, and FOXO1 priming is also important for maintaining fasting blood glucose levels. Mechanistically, suppression of glucose production by HSF1 loss may involve several NAD- and ATP-dependent regulatory points. First, consistent with a previous study (Miller et al., 2013), *hsf1* deletion reduces glucose output by increasing the [AMP]/[ATP] ratio to attenuate cAMP–PKA and glucagon-induced signaling. Second, the decrease in ATP levels caused by HSF1 loss can predominately impact the rate of hepatic glucose production by attenuating the activity of ATP-driven gluconeogenic enzymes (Foretz et al., 2010). Another possibility supported by our data is the activation of AMPK through cellular energy status changes that inhibit gluconeogenic gene expression. Finally, the predicted effect of *hsf1* deletion on loss-of-function acetylation of PGC-1α and FOXO1 can contribute to a greater suppression of glucose output (Qiang et al., 2010).

Arguably, changes in ATP supply have been linked to numerous disease conditions, particularly those that influence translation and protein folding. In addition to the high-energy–demanding systems for protein synthesis and folding, the cell needs to tightly adjust synthesis and usage to ATP levels to survive, especially under energy-limiting conditions. Our finding that HSF1 ablation provokes a systemic cellular response to adapt mTORC1-mediated protein translation to energetic stress supports a model by which mTORC1 activity is controlled directly by ATP levels (Dennis et al., 2001) or indirectly by AMPK activation (Hardie et al., 2012). However, perturbations in ATP production might have a direct negative impact on energy-sensitive steps of the protein synthesis machinery, including charging aminoacyl-tRNAs and recycling nucleotides for mRNA synthesis (Jewett et al., 2009). Another feature associated with loss of HSF1 is JNK activation and suppression of mTORC1-mediated translation, a process proposed to ensure optimal cellular survival under proteostatic stress (Su et al., 2016). However, HSF1 might not regulate mTORC1 signals predominantly through JNK in our model, because our data did not reveal a profound impact of HSF1 loss on nutrient-induced p-JNK levels (unpublished data). The intriguing possibility that the inhibition of mTORC1 activity represents a bona fide regulatory mechanism for HSF1 to optimize bioenergetic functions by selective translation of metabolic-related mRNAs (Morita et al., 2013) deserves further investigation.

In the current investigation, analysis of fatty acid metabolism revealed a marked attenuation of lipid synthesis but a slight decrease in FAO in the livers of *hsf1*$^{-/-}$ mice. Because diminished sirtuin activity causes alterations in lipid homeostasis associated with reduced FAO and increased hepatic lipid content, our contrasting findings suggest that additional mechanisms may exist in the adaptive energy strategy associated with HSF1 ablation to balance ATP demand with ATP supply. For example, AMPK-mediated reprogramming of lipid metabolism could act to convey the energy-saving signal to an enzymatic reaction regulating this response. A diminished intracellular ATP level might also be an inhibitory signal for ATP-requiring steps of lipid synthesis.

In summary, the findings suggest coordination of energy-consuming and producing processes for glucose, protein, and lipid metabolism that underpin important biological effects of HSF1-mediated energy control programs. The results prompt speculation that targeting HSF1 activity may offer a strategy for the treatment of metabolic diseases such as diabetes as well as interfere with cancer progression without compromising normal cell viability and function.

Materials and methods

Animals

Hsf1$^{-/-}$ mice were previously described (Zhang et al., 2002). Both *hsf1*$^{-/-}$ and *hsf1*$^{+/+}$ control littermates were of mixed C57BL/6-129SvPas F1 genetic background. *Hsf1*$^{f/f}$ and hepatocyte-specific *hsf1*-deletion mice on a C57BL/6J genetic background for at least nine generations are described in the following paragraph. C57BL/6J-Alb-cre mice were purchased from The Jackson Laboratory. Mice were fed ad libitum and kept in 12-h light and dark cycles. Unless otherwise indicated, mice at 2–3 mo of age were used. Animal care and experiments were performed in accordance with the guidelines of the Institutional Animal Care and Use Committee and National Institutes of Health guidelines.

Generation of *hsf1*$^{f/f}$ and liver-specific *hsf1*$^{-/-}$ mouse strains

To generate mice conditionally expressing *hsf1* (*hsf1*$^{f/f}$), a targeting vector was designed in which the neomycin gene with one *loxP* site at the distal end was inserted into intron 3 of the *hsf1* allele. The proximal *loxP* site was inserted into intron 1. Expression of cre recombinase deletes the targeted exons 2 and 3 and generates a defective gene allele, leading to complete disruption of HSF1 protein expression. For the construction of the targeting vector, a 4.2-kb proximal fragment, an 811-bp floxed fragment, and a 3.2-kb distal fragment were amplified by PCR from a bacterial artificial chromosome clone (PR23-266H9; BAC PAC Resources Center, Oakland Research Institute) containing the *hsf1* gene. The neomycin gene was flanked by two Frt sites, allowing the removal of the drug selection marker from the targeted locus through a flippase-mediated recombination event. The targeting DNA construct, introduced into the XhoI site of the phage DNA vector λDASHII-254-

2TK, was flanked by two thymidine kinase genes for drug negative selection (Zhang et al., 2002). The final vector was linearized with NotI, sequenced, and transfected into 129Sv/Ev embryonic stem cells. Embryonic stem cell clones with the floxed *hsf1*-targeted locus verified by Southern blot analysis were microinjected into blastocysts, and chimeric mice were crossed with C57BL/6J mice to generate $hsf1^{f/w}$ mice. To remove the neomycin cassette, $hsf1^{f/w}$ mice were crossed with an Flp-deleter strain (The Jackson Laboratory).

For hepatocyte-specific disruption of HSF1, $hsf1^{f/f}$ mice on a C57BL/6J genetic background (at least four generations) were crossed with alb-cre mice (Postic et al., 1999; The Jackson Laboratory) to generate $hsf1^{f/f}$-Alb-Cre$^+$ (designated as L-$hsf1^{-/-}$ mice) or $hsf1^{f/f}$ (WT) littermates, which were used as controls.

Western blotting analysis

Tissues that were snap frozen in liquid N_2 were homogenized in RIPA buffer containing protease and phosphatase inhibitors cocktail (Roche and Thermo Fisher Scientific), protein extracted, and then subjected to Western blotting. Equal amounts (30 µg) of protein were loaded onto minigels (Bio-Rad Laboratories) and transferred onto a polyvinylidene fluoride membrane using established protocols. Samples were probed for the indicated proteins as described previously (Jin et al., 2011) using the antibodies listed in the following section.

Antibodies

The following primary antibodies were used in this study: mouse HSP70 (mAb; SMC-100A/B; StressMarq Biosciences Inc.); rabbit CREB2 (sc-200), rabbit P62 (sc-25523), rabbit Ac-FRKH (FOXO1; sc-49437), goat ATF4 (sc-7583), rabbit XBP1 (sc-7160), rabbit PGC1α (sc-13067), rabbit PGC1β (sc-67286), goat ATP5α (C15; sc-49162), rabbit UQCRC2 (sc-292924), goat CD38 (sc-7049), mouse OPA1 (mAb; sc-393296), rabbit NAMPT (sc-67020), mouse (mAb) α-tubulin (sc-5286), mouse (mAb) β-actin (sc-47778), and goat γ-tubulin (sc-7396; Santa Cruz Biotechnology, Inc.); mouse (mAb) NDUFA9 (ab147130) and mouse (mAb) MTCO1 (ab14705; Abcam); rabbit β-tubulin (2376-1; Epitomics and Abcam); mouse (mAb) PARylation (AG-20T-0001; AdipoGen); rabbit CRTC2 (ST1099; EMD Millipore); rabbit AMPK (2603), rabbit phospho-AMPK(Thr172) (2535), rabbit SDHA (5839), rabbit HSP60 (12165), rabbit Ac-K (acetylated antibody; 9441), rabbit HSF1 (4356), rabbit FOXO1 (2880), rabbit p-FOXO1 (Ser256; 9461), rabbit FOXO3a (12829), rabbit p-AKT (Ser473; 4060), rabbit p-AKT (Thr308; 2965), rabbit AKT (9272), mouse (mAb) p-CREB (Ser133; 9196), rabbit PKA substrate (RRXS/T, 9624; 9621), rabbit PARP1 (9532), rabbit GRP78 (3177), rabbit LC3BI/II (2775), rabbit beclin 1 (3738), rabbit BAX (2772), rabbit pDRP1 (S616; 3455), rabbit DRP1 (8570), rabbit p-mTOR (S2448; 2971), rabbit mTOR (2972), rabbit p-Raptor (S792; 2083), rabbit Raptor (2280), mouse (mAb) p-p70SK (T389; 9206), rabbit p70SK (9202), rabbit p-S6R (S240/244; 5364), rabbit S6R (2217), rabbit p-4E-BP1(T37/46) (2855), rabbit 4E-BP1(S65) (9451), rabbit 4E-BP1(T70) (9455), rabbit 4E-BP1 (9452; Cell Signaling Technology), rabbit TFAM (GTX112760), and rabbit NDUFS3 (GTX105835; GeneTex); rabbit SOD2 (SOD-110; Assay Designs/Stressgen), mouse (mAb) MFN1 (831101), and mouse (mAb) MFN2 (820301; BioLegend).

Hepatocyte isolation

Primary hepatocytes were isolated via two-step collagenase perfusion and isolation techniques (Seglen, 1976) using liver perfusion media and liver digest buffer. Cells were allowed to attach for 2–3 h on collagen-coated plates in DMEM containing 4.5 g/liter glucose and supplemented with 10% FBS, 2 mM sodium pyruvate, and 2% penicillin and streptomycin. After attachment, the medium was replaced, and the cells were incubated overnight before used for treatment with compounds as specified in the analyses.

Histology and immunohistochemistry

Livers were fixed in 4% paraformaldehyde in phosphate-buffered saline for at least 7 d and embedded in paraffin. Hematoxylin and eosin staining was performed on 7-µm paraffin sections. For immunohistochemistry analysis, tissues were deparaffinized in xylene and rehydrated in a series of alcohol and water mixtures. Antigen retrieval was performed in 10 mM sodium citrate, pH 6.0, at 94°C for 30 min. Tissue sections were blocked in 3% BSA and then incubated with primary antibody overnight at 4°C, biotin-conjugated secondary antibody for 1 h at 25°C, and ExtrAvidin and alkaline phosphatase substrate for 30 min at 25°C. Sections were then developed with FAST Red (Roche) and counterstained with hematoxylin. Image acquisition was performed on an AxioVision Imager fluorescent microscope (ZEISS) supported with AxioCam HRC camera (ZEISS) using a 40× objective lens (NA 0.75). AxioVision REL 4.8 software was used for data analysis.

EM

EM analyses were performed at the High Resolution Electron Microscopy Facility of Medical College of Georgia at Augusta University. Livers were in situ fixed by perfusion with 2% glutaraldehyde in 0.1 M sodium cacodylate buffer, pH 7.4, postfixed with 2% $mOsO_4$ (also in sodium cacodylate buffer) for 1 h. After dehydration, tissues were embedded in epon-Araldite resin. 70-nM thin sections were cut on a MT-7000 ultramicrotome and collected on copper grids. Sections were stained with uranyl acetate and lead citrate and examined under a JEM-1200 EXII transmission electron microscope (JEOL USA Inc.). Images were captured with an UltraScan 4000 CCD camera and First Light Digital Camera Controller (Gatan Inc.).

Metabolic studies in animals and hepatocyte cultures

Glucose and pyruvate tolerance tests were performed after overnight fasting (16 h) and glucagon test after 6 h fasting. Animals were injected i.p. with 2 g glucose per kilogram body weight, 2 g/kg sodium pyruvate, or 10 µg/kg glucagon, and blood glucose levels were measured using an automated glucose monitor (Bayer HealthCare LLC). For assays showing effects of glucagon on p-CREB levels in liver, 4-h-fasted mice were injected with 30 µg glucagon per kilogram body weight via the inferior cava, and livers were collected for immunostaining or Western blotting analysis after 10 min. For in vivo insulin signaling studies, mice were injected i.p. with insulin at 0.75 U/g body weight, and livers were removed 10 min after injection.

In vitro glucose production studies were performed in primary hepatocytes cultured in DMEM with 10% FBS overnight. Cells were incubated for 4 h in glucose and phenol-red-free DMEM without serum, supplemented with 2 mM pyruvate and 20 mM lactate, 100 nM glucagon, 10 µM forskolin, or 100 mM Bt2-cAMP. Glucose output was determined using a colorimetric assay kit (Eton Bioscience Inc.).

Mitochondrial dynamics and quantification of mitochondrial parameters

For mitochondria analyzes, random EM sections of hepatocytes cut throughout the middle of the cell body were analyzed. Most of these sections contained the nucleus. AxioVision REL 4.8 software was used to evaluate the morphology of each individual mitochondrion in the digital images. Mitochondria cross-sectional areas were used to measure mitochondria size and mitochondria AR (major axis divided by minor axis). AR was used as a parameter of mitochondria shape description. Mitochondria density was estimated by counting the number of mitochondria per field of view area. Mitochondria coverage

was estimated by dividing the total area of mitochondria by the field of view area. Probability plots were used to estimate changes in mitochondria size and shape and statistical differences were tested using the Kolmogorov–Smirnov test. Slices containing hepatocyte cytosol that were not cut across the middle of the cell were also included in this analysis. Mitochondria mass was measured by MitoTracker staining and mtDNA content by quantitative PCR. For mitochondrial potential and reactive oxygen species measurements, primary hepatocytes incubated with medium containing a 1-mM (low) or 25-mM (high) glucose concentration for 1.5 h were stained with 50 mM TMRE (Molecular Probes), 5 µM MitoSOX, or 5 µM dihydroethidium for 30 min at 37°C (protected from light) and analyzed by FACS. The susceptibility of hepatocytes to induced mitochondrial dysfunction was assayed by measuring mitochondrial membrane potential by TMRE staining of cells subjected to same conditions as above and treated with 10 µM of the protonophore carbonyl cyanide *m*-chlorophenyl hydrazone for 30 min.

Mitochondria and nuclear isolation

Isolation of mitochondria from the primary hepatocytes or liver tissues was performed using a commercially available kit (catalog number 89874; Thermo Fisher Scientific). In brief, liver tissues or hepatic cells were homogenized in 2 ml mitochondria isolation buffer (70 mM sucrose, 210 mM mannitol, 5 mM Hepes, 1 mM EGTA, pH 7.2, and 0.5% BSA). The homogenates were centrifuged for 10 min at 800*g* at 4°C, and the supernatant was collected for additional centrifugation at 8,000*g* for 10 min at 4°C. The resulting pellet fraction containing the mitochondria fraction was resuspended, and the amount of protein was measured. Nuclear cell fractions were separated with commercial kit following the manufacturer's protocol (89841; Thermo Fisher Scientific).

Mitochondrial complex activities and respiration assays

OCR and ECAR were measured in hepatocytes using a XF96 Extracellular Flux Analyzer (Seahorse Bioscience). Cells were seeded on collagen-coated XF96 plates at 4×10^3 cells per well and cultured in DMEM containing 10% FBS overnight, rinsed twice, and kept in 100 µl XF medium for 1 h (nonbuffered XF base medium containing 25 mM glucose, 2 mM L-glutamine, and 1 mM sodium pyruvate). Three OCR measurements were obtained under basal conditions and upon sequential injection of 2 µM oligomycin, 2 µM fluoro-carbonyl-cyanide phenylhydrazone (FCCP), and 0.5 µM rotenone plus 0.5 µM antimycin A. OCR values were calculated from 3-min measurement cycles. The OCR measurements were adjusted to cell numbers. Glycolysis was assessed by analyzing ECAR in hepatocytes cultured in glucose-free medium after sequential addition of 10 mM glucose, 2 µM oligomycin, and 100 mM 2-deoxyglucose.

Mitochondrial FAO measurements were performed on primary hepatocytes seeded on collagen-coated XF96 plates at 4×10^3 cells per well and allowed to attach for at least 3 h. Before the assay, cells were rinsed twice and incubated in 135 µl assay medium per well (FAO medium containing 111 mM NaCl, 4.7 mM KCl, 1.25 mM $CaCl_2$, 2 mM $MgSO_4$, 1.2 mM NaH_2PO_4, 2.5 mM glucose, 0.5 mM carnitine, and 5 mM Hepes, pH 7.4) for 45 min at 37°C. 30 µl per well 1 mM BSA-conjugated palmitate or BSA as control was added, and OCR measurements were obtained under basal conditions and upon sequential injection of 2 µM oligomycin, 2 µM FCCP, and 0.5 µM rotenone plus 0.5 µM antimycin A.

The sequential electron flow through different ETC complexes was determined by monitoring OCR in isolated liver mitochondria and sequential injections of rotenone, succinate, antimycin, or ascorbate and TMPT as described in the manufacturer's technical manual (Seahorse Bioscience). Specifically, a buffer containing 10 mM pyruvate/2 mM malate with 4 µM FCCP was used to determine electron flow starting from complex I. Subsequent injections of 2 µM rotenone, 10 mM succinate, 4 µM antimycin A, and 100 µM TMPD/10 mM ascorbate was used to determine electron flow through complex II and complex IV, respectively. For this assay, 5 µg mitochondrial protein per well was used. OCR obtained in each step of the protocol was normalized by the mitochondrial protein content of the liver samples. Data were analyzed using XF software (Wave 2.2) and displayed as OCRs (picomoles per minute per well) following the Seahorse Bioscience instruction manual.

Complex I activity in isolated mitochondria was measured using a modified enzymatic assay (Spinazzi et al., 2012).

BN-PAGE

To study MC formation, BN-PAGE was performed exactly as recently described (Jha et al., 2016). In brief, 150 µg liver mitochondria isolated from WT and *hsf1*$^{-/-}$ mice were solubilized in 6 g/g digitonin (digitonin/protein ratio) and separated on a 3–12% native PAGE Bis-Tris Gell System as per the manufacturer's instructions (Thermo Fisher Scientific). After electrophoresis, gels were processed for Coomassie staining. Alternatively, 50 µg liver mitochondria solubilized in 6 g/g digitonin (protein ratio) were run on native PAGE (3–12%) gel and processed for immunoblotting with an OXPHOS antibody cocktail (457999; Invitrogen).

Metabolic labeling of cells and measurement of NAD^+ and adenine nucleotide and metabolites

ATP and AMP content in liver tissues or hepatocyte cultures were measured using an ATP/ADP/AMP determination kit (A-125; State University of New York, Buffalo) following the manufacturer's protocol. The amount was normalized to the protein content, which was determined using a protein assay (Bio-Rad Laboratories), and is presented as micromoles per gram protein. NAD^+ and NADH levels in samples from liver and hepatocyte cultures were measured using a colorimetric NAD^+/NADH assay kit (E2ND-100; BioAssay Systems). cAMP levels in primary hepatocytes were determined by using the Direct cAMP ELISA kit (Enzo Life Sciences) following the manufacturer's procedures.

For mass isotopomer distribution analysis, primary hepatocytes cultured in glucose-free DMEM supplemented with dialyzed 10% FBS were uniformly labeled with 20 mM [U-^{13}C]-6-glucose (Sigma-Aldrich) for 6 h. The samples were analyzed by gas chromatography/mass spectrometry to determine the contribution of glucose to tricarboxylic acid cycle metabolites. Data are presented as fraction of ^{13}C-labeled species within a given sample. M + 0 corresponds to an unlabeled metabolite (for example, m + 2 represents an ion labeled with two ^{13}Cs). Glucose flux analyses were performed at the Mouse Metabolic Phenotyping Center at Case Western University (Cleveland, Ohio), which is a facility sponsored by the National Institutes of Health.

Analysis of protein synthesis

For the measurement of protein synthesis in the primary hepatocytes, equal numbers of cells (2×10^5 per well) were plated on six-well BioCoat plates (Costar) overnight. After three washes, cells were cultured in with leucine-free DMEM supplemented with 5% dialyzed FBS for 30 min to depleted internal stores of leucine and then pulsed with ^{3}H-leucine in the same medium for another 30 min. Cells were washed with PBS and recultured in regular DMEM plus 10% dialyzed FBS for 30 min. After three quick washes with medium containing excess of unlabeled 2 mM leucine, 10% TCA was added to cells to precipitate the proteins, and radioactivity was measured. Protein synthesis rates were normalized to total cellular proteins prepared from parallel experiments without radioactive labeling. Experiments also were performed to measure protein synthesis after growth factor–induced signaling.

To this effect, to stimulate basal translation, hepatocytes were incubated with 100 nM insulin for 30 min before metabolic labeling with ^{3}H-leucine as described above.

For translational analysis by polysomal profiling in liver, tissue was gently homogenized in 50 mM Tris HCl, pH 7.8, 240 mM KCl, 10 mM $MgSO_4$, 5mM DTT, 250 mM sucrose, 2% Triton X-100, 90 µg/ml cycloheximide, and 30 U/ml RNasin using a glass douncer. 100 µg/ml heparin was added to the liver extract. After clarification by centrifugation 12,000 rpm for 10 min at 4°C, 5 mg protein was loaded on a 15–50% sucrose gradient dissolved in 25 mM Tris HCl, pH 7.4, 25 mM NaCl, 5 mM $MgCl_2$, and 1 mM DTT and run at 39,000 rpm (190,000 *g*) for 3 h and 30 min with a SW41Ti swing rotor (Beckman Coulter). Gradients were fractionated, and optical density at 254 nm was continuously recorded using an ISCO fractionator (Teledyne ISCO). To calculate the ratio between polysome and monosome-free subunits, the area underlying the corresponding peaks on the profile was measured using AxioVision REL 4.8 software.

De novo lipogenesis and FAO

For lipogenesis assay, 2 h serum starved primary hepatocytes were incubated with serum-free DMEM containing 74 KBq/ml [2-^{14}C]-sodium acetate (MP Biomedicals) and 0.5 mM unlabeled sodium acetate. After 4-h incubation, cells were washed twice with PBS and then lysed with 1 N NaOH solution and incubated for 1.5 h at 65°C. The resulting aqueous solution was acidified with concentrated 12 N hydrochloric acid, and lipids were extracted with petroleum ether. Radioactivity incorporation in the total lipid fraction was counted with a liquid scintillation counter (Tri-Carb 2500; PerkinElmer). For insulin-stimulated lipogenesis measurements, hepatocytes were starved for 4 h and then incubated with DMEM containing 100 nM insulin, 74 KBq/ml [2-^{14}C]-sodium acetate, and 10 µM unlabeled sodium acetate for 2 h. After lysis of the cells, lipids were extracted and radioactivity was counted.

Hepatic FAO was determined by the liberation of ^{3}H2O from [^{3}H]-oleic acid according to a procedure described previously (Harada et al., 2007; Sengupta et al., 2010) with modifications. The reaction mixture was Krebs–Ringer bicarbonate buffer containing 1 mM [^{3}H]-BSA-oleic acid (final concentration of 1 µCi/mM; Sigma-Aldrich) and 4% BSA, which was aerated with 5% CO_2 for at least 30 min before use. Approximately 40-mg liver slices were incubated in individual wells of a 24-well plate with the reaction mixture (total volume of 1 ml) at 37°C and 5% oxygen for 2 h After the incubation period, the supernatant was precipitated twice with 10% TCA followed by a centrifugation at 3,000*g* for 5 min. 1.5 ml of the supernatant was transferred to a 1.5-ml microfuge tube with no cup. Tubes were placed in scintillation vials that contained 2 ml of water, wrapped in aluminum foil, and incubated at 55°C for 18 h. The vials were then cooled at 4°C for 30 min, the tubes were removed, and the levels of $^{3}H_2O$ were measured with a liquid scintillation counter (Wallac 1450 MicroBeta Trilux; PerkinElmer).

ChIP quantitative PCR

ChIP quantitative PCR experiments were performed using a ChIP assay kit (EMD Millipore), according to manufacturer's instructions and as described in a previous report (Mendillo et al., 2012). One million cells or 50 mg liver tissue (minced in small pieces) were cross-linked with 1% formaldehyde for 10 min at 37°C. Cells were washed twice with PBS containing protease inhibitor cocktail (1 mM PMSF, 1 µg/ml aprotinin, and 1 µg/ml pepstatin A), pelleted, resuspended in 200 µl lysis buffer (1% SDS, 10 mM EDTA, and 50 mM Tris, pH 8.1), and sonicated in a ultrasonic processor (Sonicator 3000; Misonix) to a DNA size of ∼500 bp that was confirmed by agarose gel electrophoresis. Samples were precleared with protein A agarose beads and then immunoprecipitated with HSF1 antibody (sc-9144; Santa Cruz Biotechnology, Inc.), or a rabbit IgG antibody as a control, at 4°C for 16 h. Samples from *hsf1*$^{-/-}$ mice were used as an additional assay control. Chromatin protein–DNA complexes were eluted twice from the agarose beads by adding elution buffer (1% SDS, 0.1 M $NaHCO_3$, pH 8.0) at room temperature for 15 min. Cross-linking was reverse by heating at 65°C for 4 h. DNA fragment were purified by phenol/chloroform and ethanol precipitation and the putative HSE site present in the mouse nampt or hsp70 promoters were amplified by quantitative PCR with the following primers: *Nampt* forward, 5′-CCCGCATAA AACAGCCTAAA-3′; *Nampt* reverse, 5′-AACTGGCACAGACTG CATCA-3′; *Hsp70* forward, 5′-TCCAGAGACAAGCGAAGACA-3′; and *Hsp*70 reverse, 5′-GAGTAGGTGGTGCCCAGGT-3′.

Quantitative real-time PCR for mRNA and DNA quantification

Total RNA was isolated from liver tissue using TRIzol (Invitrogen) and reverse transcribed using the Iscript cDNA synthesis kit (170-8891; Bio-Rad Laboratories). Quantitative real-time PCR reaction was performed using iQ SYBR Green Supermix (Bio-Rad Laboratories) on a Stratagene Mx 3000P QPCR system. Relative quantitative plots were constructed for quantity of RNA input and for each gene of interest. Quantitative real-time PCR was performed using gene-specific primers (primer sequences are presented in Table S1).

To measure mtDNA content (marker of mitochondrial number), liver tissue was homogenized using 1× PBS and digested in a lysis buffer containing Proteinase K overnight. Genomic and mitochondrial DNA were extracted by conventional phenol-chloroform method. Quantitative PCR was performed using mitochondrial DNA (cytochrome *c*) and genomic DNA (b-actin)–specific primers (Cytb forward, 5′-CGCTTT CCACTTCATCTTACC-3′; Cytb reverse, 5′-CCTGTTGGGTTGTTT GATCC-3′; Actb forward, 5′-TTTCTGTCACTCTTCTCTTAGGT-3′; and Actb reverse, 5′-AGGTCTTTACGGATGTCAAGG-3′).

Statistical consideration

All analyses were performed with at least five to ten mice. Data are presented as mean ± SD. Statistical significance between experimental groups was assessed by an independent Student's *t* test, and $P < 0.05$ was considered significant.

Online supplemental material

Fig. S1 describes the strategy used to generate and characterize mice with a conditional *hsf1* allele. Fig. S2 evaluates the effects of HSF1 loss on hepatic NAD^+-consuming PARP and CD38 activities and profiles the mRNA levels of key enzymes in NAD^+ biosynthesis as well as of dehydrogenases that reduce NAD^+ to NADH. Fig. S3 describes the effects of HSF1 loss on hepatic mitochondrial dynamics and mitophagy as well as mitochondrial DNA replication and unfolded protein response. Fig. S4 describes analyses on the inhibitory effects of HSF1 loss in gluconeogenesis through attenuation of glucagon- and FOXO1-mediated signaling. Fig. S5 describes a model highlighting the HSF1-dependent effects on hepatic bioenergetics and anabolic metabolic pathways, including gluconeogenesis, translation, and lipid synthesis. Table S1 lists the primers used for quantitative PCR. Table S2 lists the genes mentioned in the text.

Acknowledgments

We thank Dr. Michelle Puchowicz at Case Western Metabolic Phenotyping Center for metabolic analyses and Chao Jiang for excellent technical support.

The research was supported by National Institutes of Health grants CA062130, CA062130S1, and CA132640 (N.F. Mivechi and D. Moskophidis).

The authors declare no competing financial interests.

Author contributions: A. Qiao, X. Jin, and J. Pang acquired the data. J.P. developed the technology. D. Moskophidis and N.F. Mivechi conceived and designed the study and wrote the manuscript.

Submitted: 22 July 2016
Revised: 20 November 2016
Accepted: 30 December 2016

References

Adamietz, P. 1987. Poly(ADP-ribose) synthase is the major endogenous nonhistone acceptor for poly(ADP-ribose) in alkylated rat hepatoma cells. *Eur. J. Biochem.* 169:365–372. http://dx.doi.org/10.1111/j.1432-1033.1987.tb13621.x

Akerfelt, M., R.I. Morimoto, and L. Sistonen. 2010. Heat shock factors: Integrators of cell stress, development and lifespan. *Nat. Rev. Mol. Cell Biol.* 11:545–555. http://dx.doi.org/10.1038/nrm2938

Anckar, J., and L. Sistonen. 2011. Regulation of HSF1 function in the heat stress response: Implications in aging and disease. *Annu. Rev. Biochem.* 80:1089–1115. http://dx.doi.org/10.1146/annurev-biochem-060809-095203

Anderson, R.M., K.J. Bitterman, J.G. Wood, O. Medvedik, and D.A. Sinclair. 2003. Nicotinamide and PNC1 govern lifespan extension by calorie restriction in *Saccharomyces cerevisiae*. *Nature.* 423:181–185. http://dx.doi.org/10.1038/nature01578

Buttgereit, F., and M.D. Brand. 1995. A hierarchy of ATP-consuming processes in mammalian cells. *Biochem. J.* 312:163–167. http://dx.doi.org/10.1042/bj3120163

Cantó, C., R.H. Houtkooper, E. Pirinen, D.Y. Youn, M.H. Oosterveer, Y. Cen, P.J. Fernandez-Marcos, H. Yamamoto, P.A. Andreux, P. Cettour-Rose, et al. 2012. The NAD(+) precursor nicotinamide riboside enhances oxidative metabolism and protects against high-fat diet-induced obesity. *Cell Metab.* 15:838–847. http://dx.doi.org/10.1016/j.cmet.2012.04.022

Cantó, C., K.J. Menzies, and J. Auwerx. 2015. NAD(+) Metabolism and the control of energy homeostasis: A balancing act between mitochondria and the nucleus. *Cell Metab.* 22:31–53. http://dx.doi.org/10.1016/j.cmet.2015.05.023

Dai, C., L. Whitesell, A.B. Rogers, and S. Lindquist. 2007. Heat shock factor 1 is a powerful multifaceted modifier of carcinogenesis. *Cell.* 130:1005–1018. http://dx.doi.org/10.1016/j.cell.2007.07.020

Dennis, P.B., A. Jaeschke, M. Saitoh, B. Fowler, S.C. Kozma, and G. Thomas. 2001. Mammalian TOR: A homeostatic ATP sensor. *Science.* 294:1102–1105. http://dx.doi.org/10.1126/science.1063518

Dölle, C., J.G. Rack, and M. Ziegler. 2013. NAD and ADP-ribose metabolism in mitochondria. *FEBS J.* 280:3530–3541. http://dx.doi.org/10.1111/febs.12304

Fang, E.F., M. Scheibye-Knudsen, L.E. Brace, H. Kassahun, T. SenGupta, H. Nilsen, J.R. Mitchell, D.L. Croteau, and V.A. Bohr. 2014. Defective mitophagy in XPA via PARP-1 hyperactivation and NAD(+)/SIRT1 reduction. *Cell.* 157:882–896. http://dx.doi.org/10.1016/j.cell.2014.03.026

Foretz, M., S. Hébrard, J. Leclerc, E. Zarrinpashneh, M. Soty, G. Mithieux, K. Sakamoto, F. Andreelli, and B. Viollet. 2010. Metformin inhibits hepatic gluconeogenesis in mice independently of the LKB1/AMPK pathway via a decrease in hepatic energy state. *J. Clin. Invest.* 120:2355–2369. http://dx.doi.org/10.1172/JCI40671

Guertin, M.J., and J.T. Lis. 2010. Chromatin landscape dictates HSF binding to target DNA elements. *PLoS Genet.* 6:e1001114. http://dx.doi.org/10.1371/journal.pgen.1001114

Hahn, J.S., Z. Hu, D.J. Thiele, and V.R. Iyer. 2004. Genome-wide analysis of the biology of stress responses through heat shock transcription factor. *Mol. Cell. Biol.* 24:5249–5256. http://dx.doi.org/10.1128/MCB.24.12.5249-5256.2004

Harada, N., Z. Oda, Y. Hara, K. Fujinami, M. Okawa, K. Ohbuchi, M. Yonemoto, Y. Ikeda, K. Ohwaki, K. Aragane, et al. 2007. Hepatic de novo lipogenesis is present in liver-specific ACC1-deficient mice. *Mol. Cell. Biol.* 27:1881–1888. http://dx.doi.org/10.1128/MCB.01122-06

Hardie, D.G., F.A. Ross, and S.A. Hawley. 2012. AMPK: A nutrient and energy sensor that maintains energy homeostasis. *Nat. Rev. Mol. Cell Biol.* 13:251–262. http://dx.doi.org/10.1038/nrm3311

Hebert, A.S., K.E. Dittenhafer-Reed, W. Yu, D.J. Bailey, E.S. Selen, M.D. Boersma, J.J. Carson, M. Tonelli, A.J. Balloon, A.J. Higbee, et al. 2013. Calorie restriction and SIRT3 trigger global reprogramming of the mitochondrial protein acetylome. *Mol. Cell.* 49:186–199. http://dx.doi.org/10.1016/j.molcel.2012.10.024

Hochachka, P.W., and G.B. McClelland. 1997. Cellular metabolic homeostasis during large-scale change in ATP turnover rates in muscles. *J. Exp. Biol.* 200:381–386.

Jewett, M.C., M.L. Miller, Y. Chen, and J.R. Swartz. 2009. Continued protein synthesis at low [ATP] and [GTP] enables cell adaptation during energy limitation. *J. Bacteriol.* 191:1083–1091. http://dx.doi.org/10.1128/JB.00852-08

Jha, P., X. Wang, and J. Auwerx. 2016. Analysis of mitochondrial respiratory chain supercomplexes using blue native polyacrylamide gel electrophoresis (BN-PAGE). *Curr. Protoc. Mouse Biol.* 6:1–14. http://dx.doi.org/10.1002/9780470942390.mo150182

Jin, X., D. Moskophidis, and N.F. Mivechi. 2011. Heat shock transcription factor 1 is a key determinant of HCC development by regulating hepatic steatosis and metabolic syndrome. *Cell Metab.* 14:91–103. http://dx.doi.org/10.1016/j.cmet.2011.03.025

Karamanlidis, G., C.F. Lee, L. Garcia-Menendez, S.C. Kolwicz Jr., W. Suthammarak, G. Gong, M.M. Sedensky, P.G. Morgan, W. Wang, and R. Tian. 2013. Mitochondrial complex I deficiency increases protein acetylation and accelerates heart failure. *Cell Metab.* 18:239–250. http://dx.doi.org/10.1016/j.cmet.2013.07.002

Koopman, W.J., P.H. Willems, and J.A. Smeitink. 2012. Monogenic mitochondrial disorders. *N. Engl. J. Med.* 366:1132–1141. http://dx.doi.org/10.1056/NEJMra1012478

Liesa, M., and O.S. Shirihai. 2013. Mitochondrial dynamics in the regulation of nutrient utilization and energy expenditure. *Cell Metab.* 17:491–506. http://dx.doi.org/10.1016/j.cmet.2013.03.002

Lunt, S.Y., and M.G. Vander Heiden. 2011. Aerobic glycolysis: meeting the metabolic requirements of cell proliferation. *Annu. Rev. Cell Dev. Biol.* 27:441–464. http://dx.doi.org/10.1146/annurev-cellbio-092910-154237

Ma, X., L. Xu, A.T. Alberobello, O. Gavrilova, A. Bagattin, M. Skarulis, J. Liu, T. Finkel, and E. Mueller. 2015. Celastrol protects against obesity and metabolic dysfunction through activation of a HSF1-PGC1α transcriptional axis. *Cell Metab.* 22:695–708. http://dx.doi.org/10.1016/j.cmet.2015.08.005

Mendillo, M.L., S. Santagata, M. Koeva, G.W. Bell, R. Hu, R.M. Tamimi, E. Fraenkel, T.A. Ince, L. Whitesell, and S. Lindquist. 2012. HSF1 drives a transcriptional program distinct from heat shock to support highly malignant human cancers. *Cell.* 150:549–562. http://dx.doi.org/10.1016/j.cell.2012.06.031

Miller, R.A., Q. Chu, J. Xie, M. Foretz, B. Viollet, and M.J. Birnbaum. 2013. Biguanides suppress hepatic glucagon signalling by decreasing production of cyclic AMP. *Nature.* 494:256–260. http://dx.doi.org/10.1038/nature11808

Morita, M., S.P. Gravel, V. Chénard, K. Sikström, L. Zheng, T. Alain, V. Gandin, D. Avizonis, M. Arguello, C. Zakaria, et al. 2013. mTORC1 controls mitochondrial activity and biogenesis through 4E-BP-dependent translational regulation. *Cell Metab.* 18:698–711. http://dx.doi.org/10.1016/j.cmet.2013.10.001

Mouchiroud, L., R.H. Houtkooper, N. Moullan, E. Katsyuba, D. Ryu, C. Cantó, A. Mottis, Y.S. Jo, M. Viswanathan, K. Schoonjans, et al. 2013. The NAD(+)/Sirtuin pathway modulates longevity through activation of mitochondrial UPR and FOXO signaling. *Cell.* 154:430–441. http://dx.doi.org/10.1016/j.cell.2013.06.016

Nogueiras, R., K.M. Habegger, N. Chaudhary, B. Finan, A.S. Banks, M.O. Dietrich, T.L. Horvath, D.A. Sinclair, P.T. Pfluger, and M.H. Tschöp. 2012. Sirtuin 1 and sirtuin 3: physiological modulators of metabolism. *Physiol. Rev.* 92:1479–1514. http://dx.doi.org/10.1152/physrev.00022.2011

Oh, K.J., H.S. Han, M.J. Kim, and S.H. Koo. 2013. Transcriptional regulators of hepatic gluconeogenesis. *Arch. Pharm. Res.* 36:189–200. http://dx.doi.org/10.1007/s12272-013-0018-5

Postic, C., M. Shiota, K.D. Niswender, T.L. Jetton, Y. Chen, J.M. Moates, K.D. Shelton, J. Lindner, A.D. Cherrington, and M.A. Magnuson. 1999. Dual roles for glucokinase in glucose homeostasis as determined by liver and pancreatic β cell-specific gene knock-outs using Cre recombinase. *J. Biol. Chem.* 274:305–315. http://dx.doi.org/10.1074/jbc.274.1.305

Qiang, L., A.S. Banks, and D. Accili. 2010. Uncoupling of acetylation from phosphorylation regulates FoxO1 function independent of its subcellular localization. *J. Biol. Chem.* 285:27396–27401. http://dx.doi.org/10.1074/jbc.M110.140228

Rolfe, D.F., and G.C. Brown. 1997. Cellular energy utilization and molecular origin of standard metabolic rate in mammals. *Physiol. Rev.* 77:731–758.

Rowe, G.C., I.S. Patten, Z.K. Zsengeller, R. El-Khoury, M. Okutsu, S. Bampoh, N. Koulisis, C. Farrell, M.F. Hirshman, Z. Yan, et al. 2013. Disconnecting mitochondrial content from respiratory chain capacity in PGC-1-deficient

skeletal muscle. *Cell Reports.* 3:1449–1456. http://dx.doi.org/10.1016/j.celrep.2013.04.023

Santagata, S., M.L. Mendillo, Y.C. Tang, A. Subramanian, C.C. Perley, S.P. Roche, B. Wong, R. Narayan, H. Kwon, M. Koeva, et al. 2013. Tight coordination of protein translation and HSF1 activation supports the anabolic malignant state. *Science.* 341:1238303. http://dx.doi.org/10.1126/science.1238303

Seglen, P.O. 1976. Preparation of isolated rat liver cells. *Methods Cell Biol.* 13:29–83. http://dx.doi.org/10.1016/S0091-679X(08)61797-5

Sengupta, S., T.R. Peterson, M. Laplante, S. Oh, and D.M. Sabatini. 2010. mTORC1 controls fasting-induced ketogenesis and its modulation by ageing. *Nature.* 468:1100–1104. http://dx.doi.org/10.1038/nature09584

Spinazzi, M., A. Casarin, V. Pertegato, L. Salviati, and C. Angelini. 2012. Assessment of mitochondrial respiratory chain enzymatic activities on tissues and cultured cells. *Nat. Protoc.* 7:1235–1246. http://dx.doi.org/10.1038/nprot.2012.058

Su, K.H., J. Cao, Z. Tang, S. Dai, Y. He, S.B. Sampson, I.J. Benjamin, and C. Dai. 2016. HSF1 critically attunes proteotoxic stress sensing by mTORC1 to combat stress and promote growth. *Nat. Cell Biol.* 18:527–539. http://dx.doi.org/10.1038/ncb3335

Trammell, S.A., B.J. Weidemann, A. Chadda, M.S. Yorek, A. Holmes, L.J. Coppey, A. Obrosov, R.H. Kardon, M.A. Yorek, and C. Brenner. 2016. Nicotinamide riboside opposes type 2 diabetes and neuropathy in mice. *Sci. Rep.* 6:26933. http://dx.doi.org/10.1038/srep26933

Verdin, E. 2015. NAD^+ in aging, metabolism, and neurodegeneration. *Science.* 350:1208–1213. http://dx.doi.org/10.1126/science.aac4854

Wallace, D.C. 2005. A mitochondrial paradigm of metabolic and degenerative diseases, aging, and cancer: A dawn for evolutionary medicine. *Annu. Rev. Genet.* 39:359–407. http://dx.doi.org/10.1146/annurev.genet.39.110304.095751

Yang, H., T. Yang, J.A. Baur, E. Perez, T. Matsui, J.J. Carmona, D.W. Lamming, N.C. Souza-Pinto, V.A. Bohr, A. Rosenzweig, et al. 2007. Nutrient-sensitive mitochondrial NAD+ levels dictate cell survival. *Cell.* 130:1095–1107. http://dx.doi.org/10.1016/j.cell.2007.07.035

Yoshino, J., K.F. Mills, M.J. Yoon, and S. Imai. 2011. Nicotinamide mononucleotide, a key NAD(+) intermediate, treats the pathophysiology of diet- and age-induced diabetes in mice. *Cell Metab.* 14:528–536. http://dx.doi.org/10.1016/j.cmet.2011.08.014

Zhang, Y., L. Huang, J. Zhang, D. Moskophidis, and N.F. Mivechi. 2002. Targeted disruption of hsf1 leads to lack of thermotolerance and defines tissue-specific regulation for stress-inducible Hsp molecular chaperones. *J. Cell. Biochem.* 86:376–393. http://dx.doi.org/10.1002/jcb.10232

Zong, W.X., J.D. Rabinowitz, and E. White. 2016. Mitochondria and cancer. *Mol. Cell.* 61:667–676. http://dx.doi.org/10.1016/j.molcel.2016.02.011